NAG5-332

113 pages

IN-11567

FT889400

THE FLORIDA STATE UNIVERSITY

COLLEGE OF ARTS AND SCIENCES

SENSITIVITY ANALYSIS OF HORIZONTAL HEAT AND VAPOR TRANSFER COEFFICIENTS FOR A CLOUD-TOPPED MARINE BOUNDARY LAYER DURING COLD-AIR OUTBREAKS

by

YUWEN VAUGHN CHANG

A Thesis submitted to the
Department of Meteorology
in partial fulfillment of the
requirements of the degree of
Master of Science

Approved:

____
Professor Directing Thesis

____

____

April, 1986

(NASA-CR-177282) SENSITIVITY ANALYSIS OF HORIZONTAL HEAT AND VAPOR TRANSFER COEFFICIENTS FOR A CLOUD-TOPPED MARINE BOUNDARY LAYER DURING COLD-AIR OUTBREAKS M.S. Thesis (Florida State Univ.,
N86-27836
Unclas
G3/46 43227

SENSITIVITY ANALYSIS OF HORIZONTAL HEAT AND VAPOR TRANSFER COEFFICIENTS FOR A CLOUD-TOPPED MARINE BOUNDARY LAYER DURING COLD-AIR OUTBREAKS

ABSTRACT

Yuwen Vaughn Chang, M.S.
The Florida State University, 1986

Major Professor: Steven A. Stage, Ph.D.

The effects of external parameters on the surface heat and vapor fluxes into the marine atmospheric boundary layer (MABL) during cold-air outbreaks are investigated using the numerical model of Stage and Businger (1981a). These fluxes are nondimensionalized using the horizontal heat (g_1) and vapor (g_2) transfer coefficient method first suggested by Chou and Atlas (1982) and further formulated by Stage (1983a).

In order to simplify the problem, the boundary layer is assumed to be well mixed and horizontally homogeneous, and to have linear shoreline soundings of equivalent potential temperature and mixing ratio. Modifications of initial surface flux estimates, time step limitation, and termination conditions are made to the MABL model to obtain accurate computations.

The dependence of g_1 and g_2 in the cloud topped boundary layer on the external parameters (wind speed, divergence, sea surface temperature, radiative sky temperature, cloud top radiation cooling, and initial shoreline soundings of temperature, and mixing ratio) is studied by a sensitivity analysis, which shows that the uncertainties of horizontal transfer coefficients caused by changes in the parameters are reasonably small. Therefore, the surface heat and vapor fluxes are also weakly dependent on the external parameters, and can be well-estimated by the horizontal transfer coefficient method even from rather poor measurements.

It is found numerically in this paper that the concept of horizontal transfer coefficients can be applied to both cloud-free and cloud-topped regions of the marine boundary layer for the estimation of surface fluxes at any given fetch. Although it is best to estimate fluxes by direct computation using the numerical MABL model whenever possible, values of g_1 and g_2 are close to those obtained analytically for the dry case. Thus, the analytical solutions of the horizontal transfer coefficients can be used to obtain surface flux estimates which are accurate enough for many purposes without actually numerically integrating the MABL model.

ACKNOWLEDGEMENTS

This thesis was made possible by the support of NASA grant NAG 5-332. The topic discussed in this thesis was suggested by Dr. Steven A. Stage whose continuous guidance and mental support have been indispensible.

My thanks to Professor Steven A. Stage for his patience and helpful guidances which have lead me into a much better level of research . It is beyond the words of my thanks. My thanks also to Professor James J. O'Brien, Jon E. Ahlquist, and Steven A. Stage for the many helpful suggestions they have made during my pursuit of this degree, and for the improvement of this thesis work due to them. My thanks to Thomas Schonher, Dale Allen and Simmule Turner for correcting this manuscript.

Lastly, a very special thank you to my parents Mr. D. Y. Chang and Mrs. H. L. Chang and my sisters for their love, support, and encouragement at all stages of my education.

TABLE OF CONTENTS

LIST OF TABLES

LIST OF FIGURES

CHAPTER 1 INTRODUCTION AND MOTIVATION

Cold-air outbreaks often occur after a frontal passage during winter since large temperature gradients exist in the frontal area. Once the cold front passes over warm water, the large temperature and vapor contrasts between the warm water surface and the cold and dry arctic air result in abnormally strong surface heat and vapor fluxes into the boundary layer. These fluxes are critical factors in the boundary layer modification and are important as energy sources for atmospheric motions above the boundary layer. Atlas et al. (1983) suggested that the large energy input to the atmosphere during cold air outbreaks associated with mesoscale convergence zones, and shoreline shape might be important in cyclogenesis. Numerous studies show that brief cold air outbreaks supply a large portion of air-sea fluxes. Hence, they are very important in determining the energy budgets of sea and atmosphere during winter, late fall, or early spring.

Chou and Atlas (1982) first suggested that for any given fetch the net sensible and latent heat fluxes per unit travel are proportional to the surface temperature and mixing ratio differences between sea and shoreline.

Based on the assumptions of well mixed boundary layer and horizontal homogeneity in the shoreline direction, Stage (1983a) derived analytic solutions for the fluxes before the cloud edge. His solutions provide a nondimensional method to parameterize the surface heat and vapor fluxes from warm water surfaces of dry (cloud-free) boundary layer during cold air outbreaks.

The goal of this paper is to extend Stage's nondimensional method (1983a) of computing dry boundary layer surface fluxes into the cloud-topped marine boundary layers during cold air outbreaks. A modified numerical version of the boundary layer model, which was first developed by Stage and Businger (1981a,b) for cold air outbreaks, is presented in this paper and used to compute the nondimensional flux parameters, horizontal heat (g_1) and vapor (g_2) transfer coefficients for both cloud-free and cloud-topped regions. Sensitivity analysis of how g_1 and g_2 are affected by the uncertainties of external parameters measured by satellite and shoreline sounding is the major approach of this study.

From the results of this work, a better understanding of the changes of heat and vapor fluxes during the layer evolution is obtained. Most of all, it is found that the uncertainties of g_1 and g_2 caused by the changes of external parameters are not very large. Therefore, the surface heat and vapor fluxes at any given fetch can be reasonably estimated by the horizontal transfer coefficient method, for most of the cold air outbreak episodes even with very poor measurement.

The technology of today can measure some of the boundary layer parameters at any point of the fetch by satellite, as discussed by Allison (1984). These parameters include surface wind speed or surface stress, integrated cloud top temperature, water surface temperature, and integrated liquid water and water vapor content in the atmosphere. By using the satellite measured data and a well-mixed boundary layer assumption, Allison's method (1984) can calculate the surface heat, vapor and momentum fluxes at any point of the fetch. However, the work done in this thesis provides a complement to Allison's work. Given shoreline sounding measurements and similar boundary layer assumptions, the surface heat and vapor fluxes between the shore and any given point can be computed. Thus, the technique verified in this thesis provides an alternate way to compute fluxes, which can be used when shoreline soundings are available, but not the satellite parameters needed for Allison's method.

Chapter 2 introduces the basic thermodynamics and equations of the Stage and Businger's model (1981a,b); and the horizontal transfer coefficient method proposed by Stage (1983a) for the parameterization of heat and vapor fluxes to the cloud edge during cold air outbreaks is also presented. g_1 and g_2 computed by the modified numerical marine boundary layer model are compared with the analytic solutions of horizontal transfer coefficient method. The result shows that the numerical and analytical solutions are identical to each other in the dry (cloud-free) boundary layer.

In chapter 3, the modified numerical model is applied to estimate the boundary layer evolution into the cloud-topped regions. The sensitivity analysis shows that changes of heat and vapor fluxes relative to the fundamental boundary layer parameters are not very large. This suggests that the horizontal transfer coefficient method is a promising way of estimating surface fluxes at any given fetch, regardless of the large measurement uncertainty of satellite and sounding data.

Finally, in chapter 4, the conclusions of this paper and outlook for further research work will be presented.

CHAPTER 2 FORMULATION OF THE MODEL

2.1 Introduction of The Model Physical Background

In this chapter, the model developed by Stage and Businger (1981a,b) to simulate the well-mixed, cloud-topped planetary boundary layer over warm water during cold-air outbreaks will be discussed. Such outbreaks frequently occur in many parts of the world during the fall and winter, especially over the western sections of midlatitude oceans off the east coasts of Asia and North America. In these regions, cold-air outbreaks combined with large air-sea temperature differences, high winds, synoptic scale convergence, and relatively cold dry air can cause much greater heat and moisture fluxes than oceanic means. So far, other studies of similar boundary layer situations include analysis of AMTEX data of cold air masses which leave China and cross the warm water of the Kuroshio, (Ninomiya 1974, 1975; Ninomiya and Akiyama 1976); Chou and Atlas's (1982) studies of cold-air outbreaks over the warm water area, off the south shore of Long Island during the winter of 1979; and Stage and

Businger's (1981a,b) studies of cold-air outbreaks over Lake Ontario from IFYGL data.

The model mentioned above for simulating the evolution of the cloud-topped marine boundary layer during cold air outbreaks is further modified and applied in my work. This model predicts all of the mean thermodynamics of the boundary layer, such as the rate of change of mean equivalent potential temperature, mean mixing ratio, and boundary layer depth following a column of air as it traverses a warm water surface .

All these changes in mixed-layer properties result from the following effects: surface turbulent fluxes of heat and water vapor, radiative warming of cloud bases and cooling of cloud tops, condensation and evaporation, entrainment of dry warm air from the inversion base, and lifting (subsidence) imposed by convergence (divergence) in the mixed layer. These processes are shown schematically in Fig. 2.1.1.

Parameterization of net sensible and latent heat fluxes per unit travel from the surface, and their evolution during cold air outbreaks are the main concern of studies in this paper. This parameterization theory was first developed by Chou and Atlas (1982). They noticed that the net surface sensible heat flux per unit travel , H_v/x, at any given distance from the shore ,

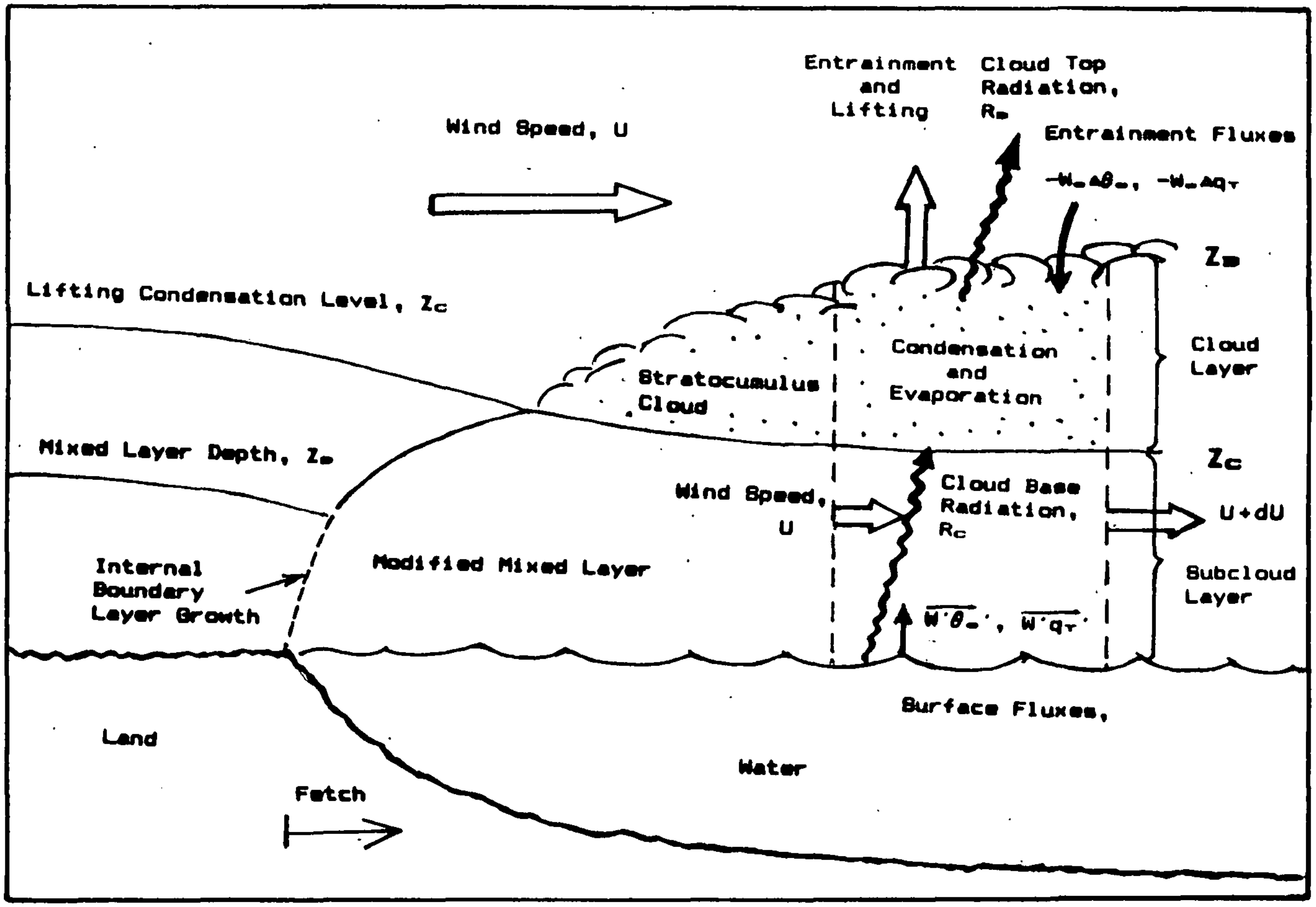

Fig.2.1.1. A schematic diagram of the evolution of marine boundary layer during cold-air outbreaks. (After Stage and Businger 1981a)

fetch, is approximately proportional to the surface temperature difference between the sea and shore. Also the net surface latent heat flux per unit travel , H_L/x, at any given fetch is approximately proportional to the surface mixing ratio difference between the sea and shore. They then suggested that these surface flux per unit travel terms can be simply expressed as horizontal transfer coefficients multiplied by the surface temperature or the mixing ratio differences.

Later in this paper, more details about how the horizontal heat and vapor transfer coefficients are affected by the fundamental parameters of the atmospheric boundary layer will be described.

2.2 Fundamental Variables and Basic Thermodynamics

The model is based on the assumption that the equivalent potential temperature θ_e and total water mixing ratio q_T are linear functions of height at the shore and are well mixed throughout the boundary layer. Therefore, the layer can be treated as a slab. Sharp jumps exist in the profiles of θ_e and q_T at the top of the mixed layer because of the inversion. Also, it is assumed that the boundary layer is horizontally homogeneous in the shoreline direction.

The vertical profiles of θ_e and q_T, and the corresponding vertical fluxes $\overline{W'\theta_e'}$, $\overline{W'q_T'}$ are shown in Fig.2.2.1. All the variables used in this model are defined below.

The independent variable is either:

t time,

or

x fetch.

The fundamental dependent variables are:

Z_e	ensemble mean mixed layer depth due to entrainment;
Z_D	ensemble mean mixed layer depth due to convergence;
θ_e	vertical and ensemble mean mixed layer equivalent potential temperature;
q_T	vertical and ensemble mean mixed layer total water vapor mixing ratio.

At the shoreline, $Z_D = 0$, and $Z_B = Z_D + Z_e = Z_e$, where Z_B is the ensembled mixed layer depth, and the initial values are specified for Z_e, θ_e, and q_T. Then all other

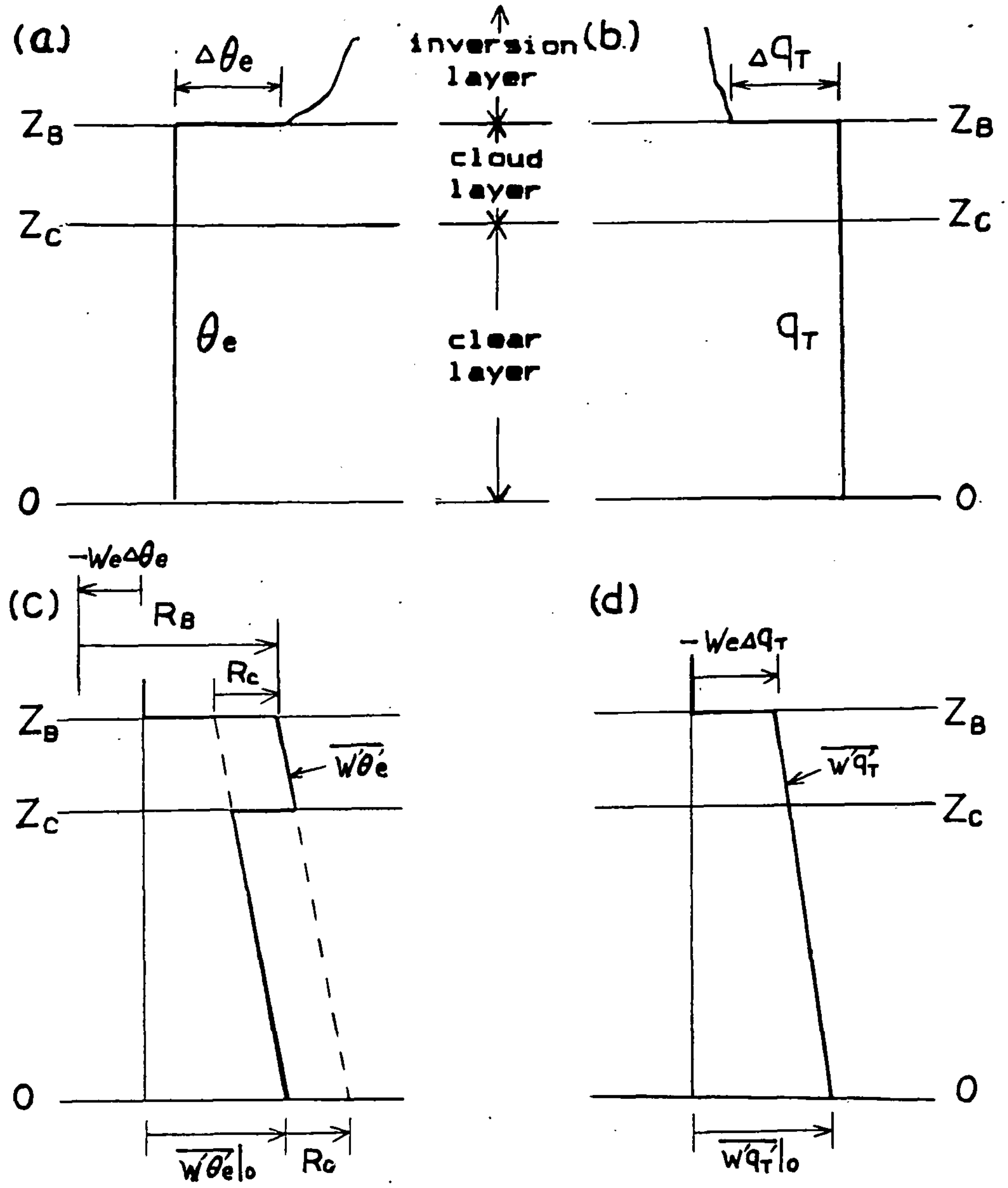

Fig.2.2.1 Profiles of idealized MABL model.(From Stage and Businger, 1981a, Fig. 3)

a. Equivalent potential temperature.(θ_e)

b. Total water vapor mixing ratio.(q_T)

c. Equivalent potential temperature flux. ($\overline{w'\theta_e'}$)

d. Total water vapor flux. ($\overline{w'q_T'}$)

variables of the boundary layer can be calculated from these fundamental variables. If applied to data, ensemble averages must be estimated by time averages in the steady-state condition; averages parallel to the shoreline with homogeneous upwind condition in that direction; or areal averages with small extent in the streamwise direction.

The basic thermodynamic properties of the model fundamental variables are shown below. The equivalent potential temperature is defined as :

$$\theta_e = \theta \exp(Lq_v / C_p T), \tag{2.2.1}$$

where L is the latent heat of evaporation of water;

C_p is the specific heat of air at constant pressure;

q_v is the water vapor mixing ratio.

An accurate approximation of (2.2.1) can be written as:

$$\theta_e \cong \theta + (L/C_p) q_v. \tag{2.2.2}$$

The total water mixing ratio is defined as:

$$q_T = q_v + q_l, \tag{2.2.3}$$

where

q_v is water vapor mixing ratio,

q_l is liquid water mixing ratio.

The Clausius-Clapeyron equation may be expressed as:

$$de = (\epsilon eL/RT_d^2)\ dT_d, \qquad (2.2.4)$$

where

ϵ is the ratio of the molecular weight of water to dry air ($\epsilon \cong 0.622$),

T_d is the dew point of the air,

e is the water vapor partial pressure of the air which can be expressed as:

$$e = Pq_v/\epsilon , \qquad (2.2.5)$$

where P is pressure of the air.

By differentiating (2.2.5) we have:

$$dq_v/q_v = de/e - dP/P, \qquad (2.2.6)$$

and by the use of (2.2.4), the ideal gas law, and the hydrostatic equation , the following equation is derived :

$$dq_v/q_v = (\epsilon L)/(RT_d^2)dT_d + (g/RT)dZ. \qquad (2.2.7)$$

We can integrate (2.2.7). If the saturation mixing ratio (q_r) corresponding to the dew point temperature (T_{dr}) is known, then the pair of related functions are inferred as:

$$Q(T) = q_r \exp(-\frac{L\epsilon}{R}(\frac{1}{T} - \frac{1}{T_r})), \qquad (2.2.8)$$

and

$$T_{do}(q) = (-\frac{R}{L\epsilon} \ln(\frac{q}{q_r}) + \frac{1}{T_{dr}})^{-1}, \qquad (2.2.9)$$

where

$Q(T)$ is the saturation water vapor mixing ratio for air at $Z=0$ and temperature T;

$T_{do}(q)$ is the dewpoint for air at $Z=0$, and water vapor mixing ratio q.

Notice that these two functions are inverses of each other, thus

$$q = Q(T_{do}(q)), \qquad (2.2.10a)$$

and

$$T = T_{do}(Q(T)). \qquad (2.2.10b)$$

For air below its saturation level, q_v is conserved, so that $dq_v = 0$, and from (2.2.7) we can derive:

$$dT_d = -(gT/L\epsilon)dZ \qquad (2.2.11)$$

by using $T \cong T_d$.

Integrating (2.2.11) as a parcel is lifted from the surface up, and assuming $T \cong$ constant,

$$T_d = T_{do}(q_v) - (gT/\epsilon L)Z. \qquad (2.2.12)$$

From (2.2.12), we see that for nonsaturated conditions the approximate dew point lapse rate is $-(gT/\epsilon L) =$ 1.76 C/km. We can define dew point potential temperature as:

$$\theta_d = T_d + \gamma Z. \qquad (2.2.13)$$

By combining (2.2.12) and (2.2.13), we have:

$$\theta_d = T_{d0}(q_v) + (\gamma - gT/\epsilon L)Z. \qquad (2.2.14)$$

Another useful quantity is liquid water potential temperature, θ_l, which is defined as:

$$\theta_l = \theta_e - (L/C_p)q_T. \qquad (2.2.15)$$

For adiabatic parcel motions θ_l is conserved because θ_e and q_T are conserved. So, from (2.2.2),(2.2.3) and (2.2.15), we know:

$$\theta_l = \theta \qquad \text{for } q_l = 0 \qquad (2.2.16)$$

(i.e. for nonsaturated air parcel, $q_l=0$).

The level at which dewpoint and temperature become equal is defined as the lifting condensation level, Z_c. This can be derived from (2.2.13),(2.2.14),(2.2.16) and $\theta_l = T + \gamma Z_c$ by assuming the parcel has $q_l = 0$ at level Z_c. Thus,

$$T_{do} - (gT/\epsilon L)Z_c = \theta_l - \gamma Z_c, \qquad (2.2.17)$$

$$Z_c = (\theta_l - T_{do})/(\gamma - gT/\epsilon L). \qquad (2.2.18)$$

The virtual potential temperature, θ_v, is defined as:

$$\theta_v = \theta(1 + (1/\epsilon - 1)q_v + q_l) \qquad (2.2.19)$$

$$= (\theta_e - (L/C_p)q_v)(1 + (1/\epsilon - 1)q_v + q_l).$$

This temperature includes the effects of both water vapor buoyancy and liquid water drag.

The last important thermodynamic property to be introduced is the dewpoint virtual potential temperature defined as:

$$\theta_{dv} = \theta_d(1 + (1/\epsilon - 1)q_v + q_l). \qquad (2.2.20)$$

2.3 Analytic Profiles of Heat and Vapor Fluxes in the Dry MABL Model

If divergence is negligibly small then the net sensible and latent heat input from a warm water surface to the atmosphere in cloud-free regions (commonly referred to as the dry boundary layer), can be computed by vertical integration from the surface to the inversion layer of the change of θ_v and q_T in soundings. This computation method is adequately only when the atmospheric divergence is negligible, because there is hardly any change of the sounding profiles above Z_B. Thus, we can express the net sensible and latent heat input to the boundary layer as :

$$H = \rho C_p \int_0^{Z_B} (\theta - \theta_{X=0}) dZ \qquad (2.3.1)$$

$$H_L = \rho L \int_0^{Z_B} (q - q_{X=0}) dZ \qquad (2.3.2)$$

where

H is the net sensible heat input,

H_L is the net latent heat input.

The analytic solution for a dry boundary layer was first developed by Stage (1983a). The more complicated condition of a cloud-topped boundary layer (called as wet boundary layer) after cloud formation during boundary layer evolution has not been solved analytically. In this section, the analytic profiles of heat and vapor fluxes before the cloud formation point will be presented. First, it is known that there is no liquid water (q_l=0) in this region, hence $q_T = q_v$. Therefore, the virtual potential temperature and virtual heat flux input to the boundary layer can be written as:

$$\theta_v = \theta(1 + (1/\epsilon - 1)q_T). \qquad (2.3.3)$$

Let

$$H_v = \rho C_p \int_0^{Z_B} (\theta_v - \theta_v \big|_{x=0}) dZ. \qquad (2.3.4)$$

Substituting (2.3.1), (2.3.2) into (2.3.3) gives

$$H_v = H + (1/\epsilon - 1)\theta_o (C_p/L) H_L. \qquad (2.3.5)$$

Next, neglecting molecular diffusion and horizontal convergence of turbulent heat fluxes, the heat conservation equation may be written as:

$$\frac{d\bar{\theta}_v}{dt} + \frac{\partial \overline{w'\theta_v'}}{\partial z} = 0. \qquad (2.3.6)$$

Integrating (2.3.6) with respect to Z, and applying boundary conditions leads to:

$$\frac{d\bar{\theta}_v}{dt} = \frac{1}{Z_B} (\overline{W'\theta_v'}\big|_o + W_e \Delta\theta_v), \qquad (2.3.7)$$

where the boundary condition for the dry boundary layer at

$Z = Z_{B-}$ and $Z = 0$ gives:

$$\overline{W'\theta_v'} \left\{ \begin{array}{lr} = \overline{W'\theta_v'}\big|_0 & \text{at } Z = 0, \\ & \\ = \overline{W'\theta_v'}\big|_{z_{B-}} = -W_e \Delta\theta & \text{at } Z = Z_{B-} \end{array} \right\} \qquad (2.3.8)$$

where

W_e is the entrainment rate,

$\Delta\theta$ is the temperature jump at the cloud top.

Now, take the z-derivative of (2.3.6). Since we assume the layer is well mixed, $\overline{\theta}_v = \theta_m$, and $\frac{\partial\theta_m}{\partial Z} = 0$ is a good approximation for this boundary layer model. Thus, (2.3.6) becomes:

$$\frac{\partial \overline{w\theta_v'}}{\partial Z} = \text{Const.} \qquad (2.3.9)$$

Ball (1960) proposed a relationship between cloud top entrainment rate and surface heat flux:

$$W_e \Delta\theta_v = A\ \overline{W'\theta_v'}\big|_0. \qquad (2.3.10)$$

$A \cong 0.2$ is a widely accepted value of the entrainment coefficient.

From (2.3.8) and (2.3.9), we know the heat flux of boundary layer:

$$\overline{W'\theta_v'} = \overline{W'\theta_v'}\big|_o (1-Z/Z_B) + \overline{W'\theta_v'}\big|_{Z_B-} (Z/Z_B) \qquad (2.3.11)$$

Further discussion of nondimensionalization of the net sensible heat and vapor fluxes per unit travel, and the analytic solutions of the evolution of these fluxes from real sounding data will be presented in the following sections of this chapter.

For the wet boundary layer case (i.e. after cloud formation), the heat and vapor fluxes become much more complicated. The radiation cooling rates (R_B) at the cloud top, and the radiation warming rates (R_C) at the cloud base have to be considered. In order to simplify the problem , R_B and R_C are assumed to be concentrated in a very thin layer near the cloud top and base and entirely within the mixed layer. Thus, the effect of the thickness of the radiative flux divergence layer near cloud top and base can be neglected (Stage and Businger, 1981b). Through a proof similar to the one above, by using the diffusion equation for the total water mixing ratio (q_T)

and the equivalent potential temperature (θ_e), we can derive:

$$\frac{dq_T}{dt} - \frac{\partial \overline{w'q_T'}}{\partial z} = 0, \qquad (2.3.12)$$

$$\frac{d\theta_e}{dt} - \frac{\partial \overline{w'\theta_e'}}{\partial z} + \frac{\partial (\frac{F_R}{\rho C_p})}{\partial z} = 0, \qquad (2.3.13)$$

where

$$\frac{\partial (\frac{F_R}{\rho C_p})}{\partial z} = 0 \qquad \text{everywhere except at } Z_C \text{ and } Z_B,$$

and

$$\lim_{\delta \to 0} \frac{F_R}{\rho C_p}\Bigg|_{Z_C-\delta}^{Z_C+\delta} = -R_C\ , \qquad (2.3.14a)$$

$$\lim_{\delta \to 0} \frac{F_R}{\rho C_p}\Bigg|_{Z_B-\delta}^{Z_B+\delta} = -R_B\ . \qquad (2.3.14b)$$

By taking the z-derivative of (2.3.12) and (2.3.13) to show that the turbulent fluxes must be linear in the cloud and subcloud regions, and then twice integrating the result using the boundary conditions, (2.3.14a) and (2.3.14b), the fluxes of total water mixing ratio ($\overline{W'q_T'}$) and equivalent potential temperature ($\overline{W'\theta_e'}$) can be expressed as (Stage and Businger, 1981b):

$$\overline{W'q_T'} = (1 - Z/Z_B)\,\overline{W'q_T'}\big|_0 - (Z/Z_B)W_e\Delta q_T, \qquad (2.3.15)$$

$$\overline{W'\theta_e'}\left\{\begin{array}{l} = (1-Z/Z_B)\overline{W'\theta'_e}\big|_0 - Z/Z_B(-W_e\Delta\theta + R_B - R_c), \\ \qquad\qquad \text{for} \quad 0 < Z < Z_c, \\ \\ = (1-Z/Z_B)(\overline{W'\theta_e'}\big|_0 + R_c) + Z/Z_B(-W_e\Delta\theta + R_B), \\ \qquad\qquad \text{for} \quad Z_c < Z < Z_B, \end{array}\right\} \qquad (2.3.16)$$

These idealized profiles of $\overline{W'q_T'}$ and $\overline{W'\theta_e'}$ are shown in Fig. 2.2.1 (c), (d) of the previous section.

In the cloud layer all the air motions are assumed to be saturated. Taking the perturbations of (2.2.2), (2.2.3), (2.2.19), $q_v' = (dQ_{SAT}/dT)\theta'$, and neglecting the small terms.

$$\theta_v' = \left(1 + \frac{\theta}{\epsilon}\frac{dq_s}{dt}\right)\left(1 + \frac{L}{c_p}\frac{dq_s}{dt}\right)^{-1}\theta_e' - \theta q_T'. \qquad (2.3.17)$$

This gives:

$$\overline{W'\theta_v'} = \beta\,\overline{W'\theta_e'} - \theta\,\overline{W'q_T'} \qquad \text{for } Z_c < Z < Z_B \qquad (2.3.18)$$

where

$$\beta = \left(1+\frac{\theta}{\epsilon}\frac{dq_s}{dt}\right)\left(1+\frac{L}{C_p}\frac{dq_s}{dt}\right)^{-1} ,$$

has a typical value of 0.5 to 0.6.

Combining (2.2.19), (2.3.15), (2.3.16) and (2.3.18) gives:

$$\overline{W'\theta_v'} \begin{cases} = (1-\frac{Z}{Z_B})\overline{W'\theta_v'}|_0 + \frac{Z}{Z_B}(R_B - R_C) - \frac{Z}{Z_B}\Delta_1 W_B, \\ \qquad\qquad \text{for} \quad 0 \leq Z < Z_C, \\ \\ = (1-\frac{Z}{Z_B})(\beta(\overline{W'\theta_B'}|_0 + R_C) - \theta\overline{W'q_T'}) + \frac{Z}{Z_B}\beta R_B - \frac{Z}{Z_B}\Delta_2 W_B, \\ \qquad\qquad \text{for} \quad Z_C \leq Z < Z_B, \end{cases} \qquad (2.3.19)$$

where

$$\Delta_1 = \Delta\theta_1 + (1/\epsilon - 1) q_T,$$

$$\Delta_2 = \beta\Delta\theta_B - (1/\epsilon - 1)\theta\Delta q_T.$$

The idealized profiles of θ_v and $\overline{W'\theta_v'}$ are shown in

Fig. 2.3.1a and b.

Further discussions of the parameterization of the net sensible and vapor fluxes per unit travel for the dry boundary layer (i.e. with no clouds) will be presented in the next section.

In this paper, the major concern is to use a numerical method which can simulate the more complicated and realistic evolution of the net sensible and latent heat fluxes from a warm water surface into cloud-topped region during the boundary layer development. Then, the numerical results will be compared to the analytical solutions to show the credibility of the numerical method used in this paper.

2.4 Flux Transfer Parameterization in the MABL

A parameterization method for the heat and vapor fluxes of the dry boundary layer, no cloud case, will be discussed in this section. This method was first proposed and solved analytically by Stage (1983a). For simplicity, this method assumes linear shoreline soundings. They are:

$$\theta_{\blacksquare,B+} = \theta_{\blacksquare 1} + \Gamma_{\theta\blacksquare} z_{B} \qquad (2.4.1)$$

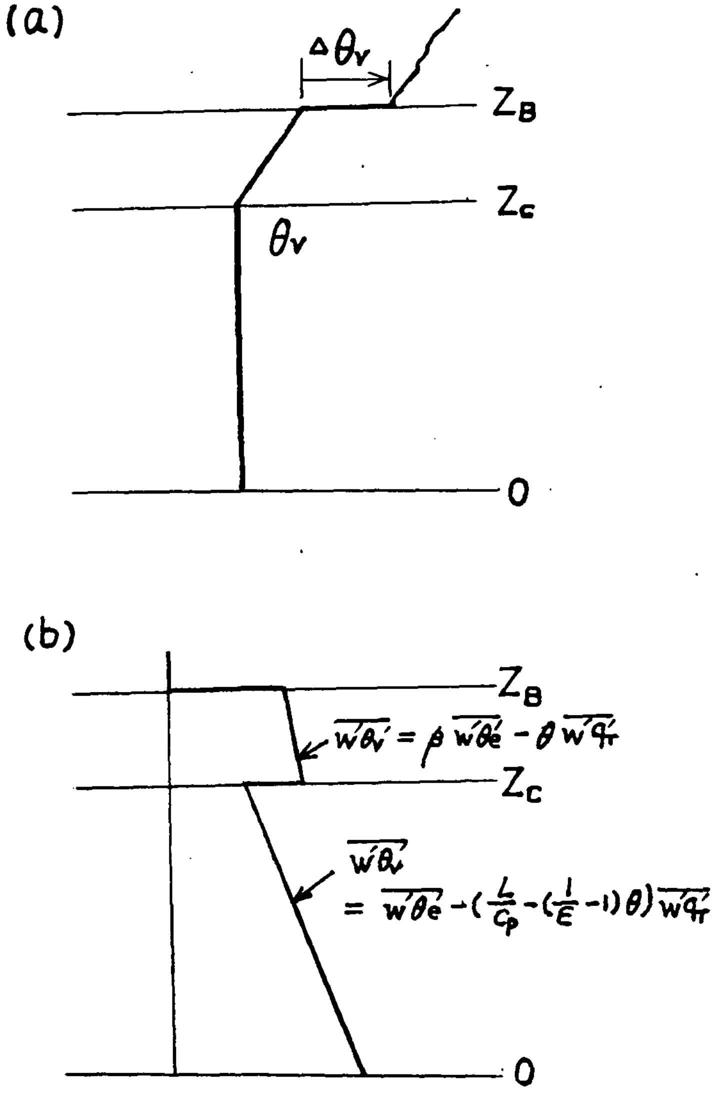

Fig.2.3.1 The idealized profiles of boundary layer.

(From Stage and Businger, 1981a)

a. Temperature. (θ_v)

b. Sensible heat flux. ($\overline{W'\theta_v'}$)

and

$$q_{T,B+} = q_{Ti} + \Gamma_{qT} Z_B. \qquad (2.4.2)$$

In the last section, we have mentioned the rate of changes of surface sensible heat and vapor fluxes. The time integrated sensible and latent heat fluxes during boundary layer evolution can be written as functions of the fetch as follows:

$$\begin{aligned} H &= (\rho C_p/U)\int_0^x \overline{W'\theta'}\Big|_0 dx \\ H_L &= (\rho L/U)\int_0^x \overline{W'q_T'}\Big|_0 dx \qquad (2.4.3) \\ H_v &= (\rho C_p/U)\int_0^x \overline{W'\theta_v'}\Big|_0 dx \end{aligned}$$

where

U is the mean wind speed in the boundary layer,

x is the fetch of boundary layer evolution as measured in the direction of U.

Chou and Atlas (1982) noticed that for any given fetch the mean net sensible heating per unit travel (H_v/x) is proportional to the surface temperature difference between air over land and sea ($\theta_{vo}-\theta_{vi}$), and that the mean net latent heating (H_L/x) per unit travel is proportional to the surface mixing ratio difference between air over land and sea ($q_o - q_1$). The analysis plotted by Chou and Atlas (1982) is reproduced in Fig.2.4.1.

Stage (1983a) parameterized H_v/x and H_L/x by using the horizontal transfer coefficient terms proposed by Chou and Atlas (1982). The net sensible and latent heating per unit travel are expressed as the horizontal transfer coefficients multiplied by ($\theta_{vo} - \theta_{v1}$) and ($q_o - q_1$).

$$H_v/x = C_1 \, (\theta_{vo} - \theta_{v1}) \, g_1 \, , \qquad (2.4.4)$$

$$H_L/x = C_2 \, (q_o - q_1) \, g_2 \, , \qquad (2.4.5)$$

where

C_1, C_2 are the constants for sensible and latent heat fluxes respectively.

The parameters of eq.(2.4.4) and (2.4.5), C_1, C_2, g_1 and g_2, have been derived by Stage (1983a) as shown below:

$$C_1 = \frac{1}{2} \rho \, C_p C_{T1} \, , \qquad (2.4.6)$$

$$C_2 = \frac{1}{2} \rho \, L C_{T1} \, , \qquad (2.4.7)$$

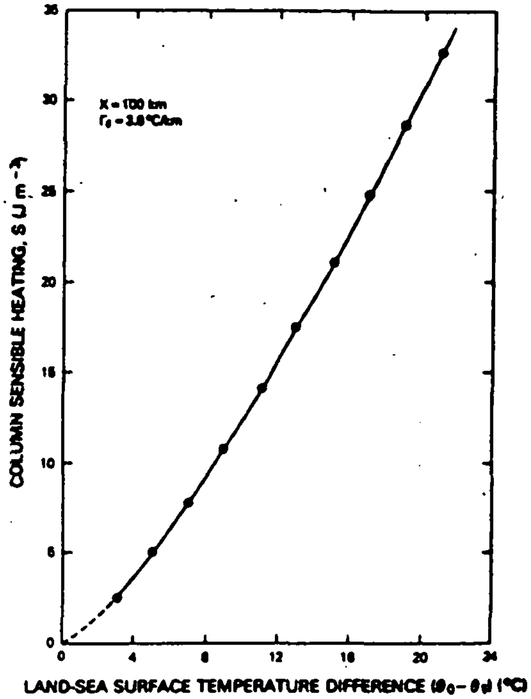

Fig.2.4.1a Variation of Mean column sensible heating versus land-sea surface temperature difference.

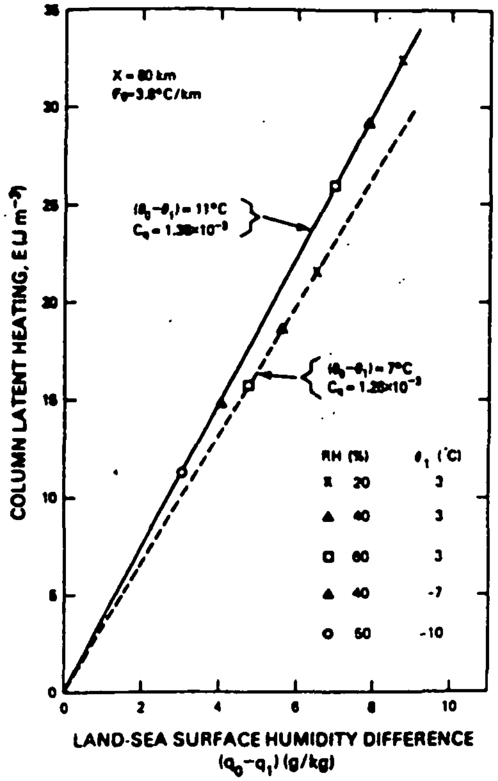

Fig.2.4.1b Variation of mean column latent heating versus land-sea surface mixint ratio difference.

where

C_{T1} is the value of C_T corresponding to an air temperature of $\theta_v = \theta_{v1}$, and a sea surface temperature of θ_{vo}. i.e. the surface temperature difference between air at shore and sea.

C_P is the specific heat of air at constant pressure,

L is the latent heat release of water vapor evaporation.

The horizontal transfer coefficients of sensible heat, g_1, and latent heat, g_2, are

$$g_1 = \eta / X , \qquad (2.4.8)$$

$$g_2 = (2(1+A)(1-F/\eta)(1-\lambda)+\lambda)\eta^2/X . \qquad (2.4.9)$$

The nondimensional terms included in the above equations are defined as follows:

(A) η : nondimensional mixed layer height, which is defined as:

$$\eta = Z/Z_{*\alpha}, \qquad (2.4.10)$$

where Z_* is a scaling height, i.e. the depth of boundary layer when fetch approaches infinity. It is defined as:

$$Z_* = \left(\frac{1+2A}{1+A}\right)(\theta_{vo}-\theta_{v1})/\Gamma_v , \qquad (2.4.11)$$

where

θ_{vo} : virtual potential temperature of the sea surface,

θ_{v1} : virtual potential temperature of the shoreline surface,

Γ_v : virtual potential temperature lapse rate in the boundary layer,

A : entrainment coefficient ($A \cong 0.2$).

(B) λ : nondimensional slope of mixing ratio, q_T, profile, which is defined as:

$$\lambda = (\Gamma_q/\Gamma_v)((\theta_{vo}-\theta_{v1})/(q_o-q_1)) , \qquad (2.4.12)$$

where

Γ_q is the mixing ratio lapse rate in the BL,

q_0 is the mixing ratio at the sea surface,

q_1 is the mixing ratio at the shoreline surface.

(C) X : nondimensional fetch of boundary layer evolution, which is defined as:

$$X = x/x_* , \tag{2.4.13}$$

where x_* is a scaling length in the fetch direction. It is defined as:

$$x_* = Z_{B\infty}/((1+A)C_{T1}) , \tag{2.4.14a}$$

from (2.4.11) we have

$$x_* = \frac{1+2A}{(1+A)^2}\left(\frac{\theta_{v0}-\theta_{v1}}{\Gamma_v C_{T1}}\right). \tag{2.4.14b}$$

(D) F : nondimensional function,

$$F = \eta - \left(1-y^{\frac{1}{1+A}} + \frac{(y-y^{\frac{1}{1+A}})}{A}\right)\frac{1}{A}, \tag{2.4.15}$$

where $y = 1-\eta$.

For $\eta << 1$ (i.e. $Z << Z_{B\infty}$), during the initial stage of the MABL evolution, (2.4.15) contains small differences between terms and is hard to compute. However, we can apply the binomial expansion in the limit situation ($\eta << 1$) to simplify the problem, such that:

$$F \cong \left(\frac{1+2A}{1+A}\right)\frac{\eta}{2} . \qquad (2.4.16)$$

By substituting (2.4.16) into (2.4.9), we can prove that $g_2 = \eta^2/\chi = g_1$, for $\eta << 1$. This has been shown in the numerical results for the initial stage run of this paper. The related plots will be presented in the later sections of this chapter.

From the definitions of horizontal sensible heat transfer coefficient g_1 and horizontal latent heat transfer coefficient g_2, (2.4.8), (2.4.9), and (2.4.13), we can see that g_1 and g_2 are functions of fetch (x).

How g_1 and g_2 change with fetch under different conditions is the major topic of the research work in this paper. Further details will be discussed in the next chapter.

From (2.4.8) to (2.4.15), nondimensionalization of vertical sensible and latent heat fluxes in MABL, all the parameters that closely affect the horizontal transfer coefficients for the dry boundary layer case are:

θ_{vo} : sea surface virtual potential temperature. It is computed from sea surface temperature (θ_O) and mixing ratio (q_{TO}).

θ_{v1} : surface virtual potential temperature at shore. It is computed from shoreline surface temperature (θ_1) and mixing ratio (q_{T1}).

Γ_v : lapse rate of virtual potential temperature. It is computed from the lapse rate of temperature (Γ_θ) and mixing ratio (Γ_{qT}).

D_1 : the divergence within the boundary layer.

D_2 : the synoptic scale divergence.

and

U : the wind speed.

All of the above parameters have been assumed constant to simplify the situation. From (2.3.6) to (2.3.19), and (2.4.3) to (2.4.5), we can see that once clouds form, g_1, g_2 are also affected by:

R_B : the radiation cooling on cloud top.

$$R_B = \frac{\sigma}{\rho C_p}\left(T_{ZB-}{}^4 - T_{SKY}{}^4 \right) ,$$

where T_{SKY} is the radiative sky temperature.

R_C : the radiation warming at cloud base.

$$R_C = \frac{\sigma}{\rho C_p}\left(T_O{}^4 - T_{ZC+}{}^4 \right),$$

where T_O is the sea surface temperature.

In conclusion, the method of deriving g_1 and g_2 with nondimensional parameters provides a means of evaluating heat and vapor fluxes with much less information than is required for the complete analysis. This method will be called the "Horizontal Transfer Coefficient Method", and the solutions of g_1 and g_2 can be solved either analytically or numerically.

As learned in this section, the advantage of the analytical solutions is that simple observations at shore and sea are adequate to solve for g_1 and g_2 at any given fetch. However, the biggest disadvantage is that this solution provides the values of heat and vapor fluxes before cloud formation only.

A schematic illustration of the analytical and numerical methods of solving the surface heat and vapor fluxes is shown in Fig.2.4.3, where g_1 and g_2 are analytically solved if the surface temperature, mixing ratio over land and ocean, and their lapse rates at shore are known. The analytical solutions of g_1 and g_2 are universal for all the cloud-free boundary layer cases. Thus, the surface heat and vapor fluxes per unit travel can be derived from (2.4.4) and (2.4.5). It is also seen from Fig.2.4.3, g_1 and g_2 are numerically solved by applying the MABL model (Stage and Businger, 1981). There are 9 external parameters needed to run the simulating boundary layer evolution model, it is good for both the

Horizontal transfer coefficients g_1 and g_2 are universal functions, which can be computed analytically and numerically.

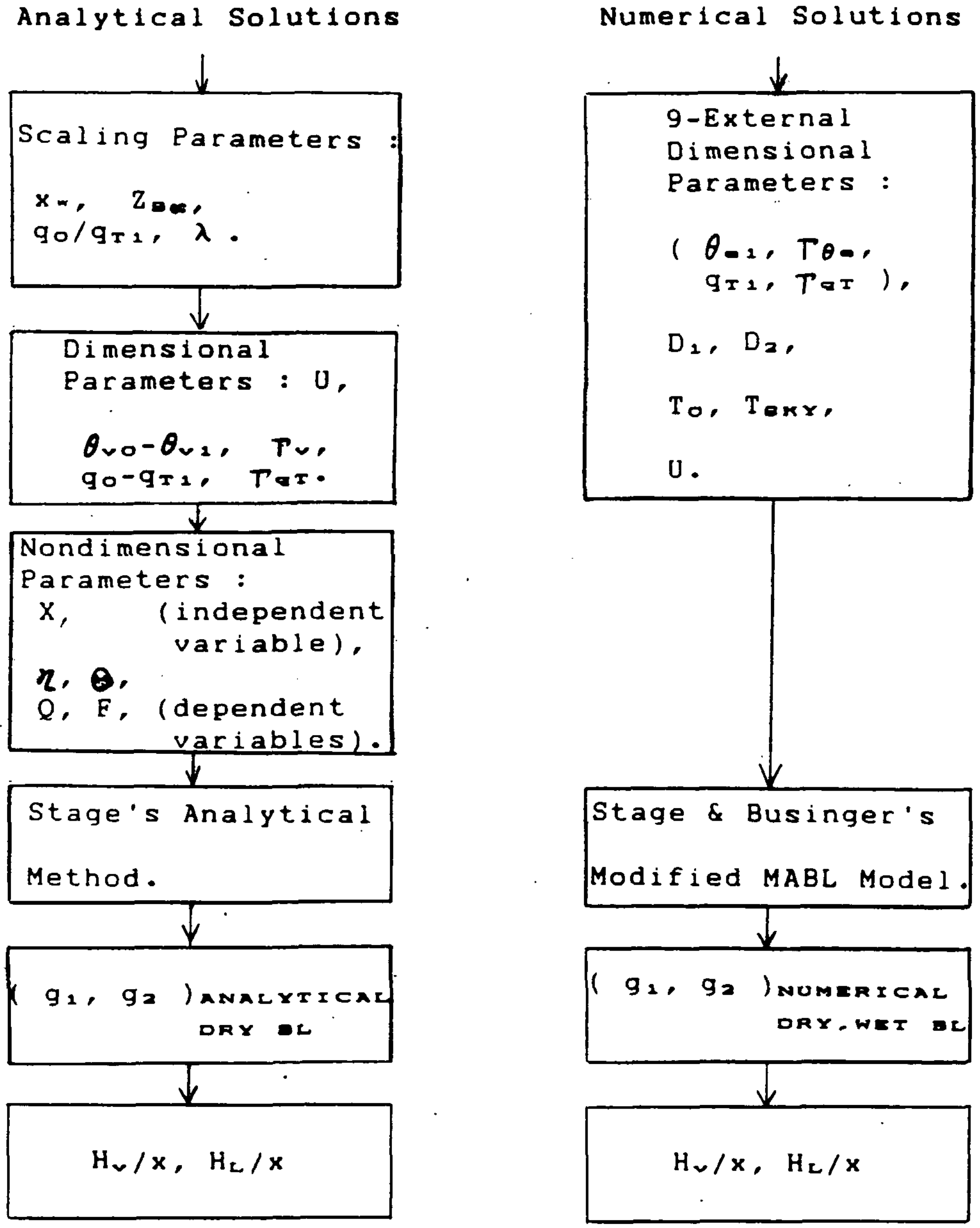

Fig.2.4.3 Flowcharts of evaluation of g_1 and g_2 and their applications to boundary layer surface fluxes approximation.

cloud-free and cloud-topped boundary layer. For the dry boundary layer, the numerical solutions of g_1 and g_2 are identical to the analytical solutions, which will be proven in the next section. For the wet boundary layer, the numerical values of g_1 and g_2 are considered to be reasonably accurate. Hence, the surface fluxes per unit travel from shore all the way to cloud-topped regions can always be estimated by running the numerical MABL model.

2.5 Comparisons Between The Numerical and The Analytical Solutions of The Model

Stage (1983a) analytically solved g_1 and g_2 of MABL evolution during cold air outbreaks for the dry (cloud-free) case. In order to compute the heat and vapor fluxes for both the wet (with cloud) and dry (no cloud) cases, a moidified numerical method from Stage and Businger's MABL model is applied in this section. This method will also be evaluated and compared with the analytical method later in this section.

The numerical method uses the same assumptions of linear conditions as the analytical model, given earlier by (2.4.1) and (2.4.2). Specification of the initial values of the fundamental variables enables the calculation of all the variables of the boundary layer.

Then the boundary layer evolution is determined by integrating the numerical model at every time step. These numerical solutions agree well with the analytic solutions in the cloud free region. They also provide relatively accurate forecasts of the heat and vapor fluxes for the cloud-topped region as will be shown in the next chapter. A comparison between the analytic and numerical solutions of horizontal transfer coefficients is presented in this section to examine how well the numerical model works.

The sounding being used here for the comparison of the two methods is the New York sounding (Stage 1979, 1981b, 1983b; Chou and Atlas 1982), taken on February 1979. It is considered to be a typical air modification situation during cold air outbreak episodes. The details of this sounding are shown in Chapter 3, Table 3.1.1. A vertical profile of the fundamental parameters of the boundary layer for the New York sounding is shown in Fig. 2.5.1 (Stage, 1979).

Although the results of the two methods shown in this section are from one particular sounding, it will be proven in Chapter 3 that the horizontal transfer coefficients determined by this numerical model are not very sensitive to changes in sounding parameters. Therefore, some general conclusions can be made with regard to the model results based on single sounding

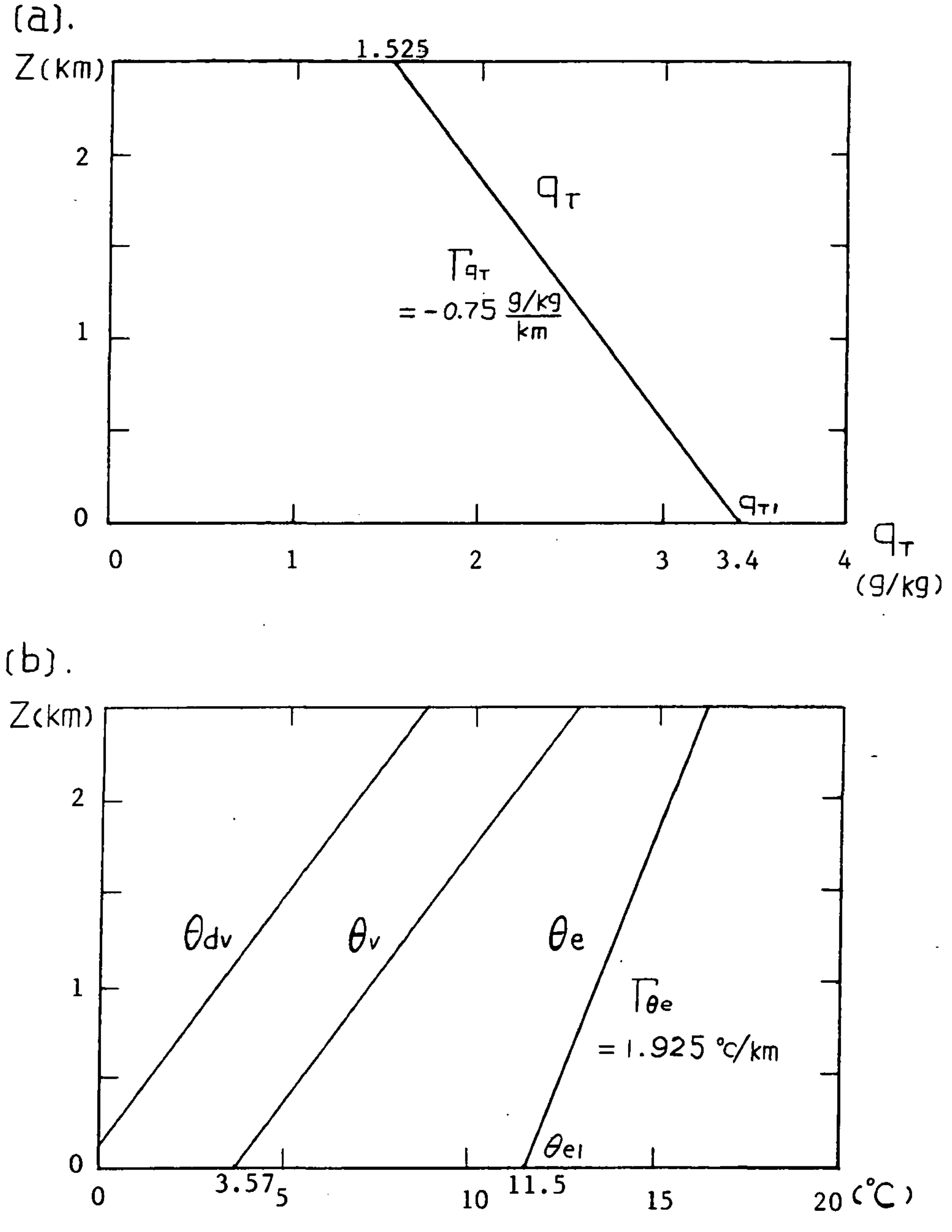

Fig.2.5.1 The MABL profiles corresponding to New York sounding. (From Stage 1979)

a. Temperature.

b. Mixing ratio.

data.

The analytic solutions of horizontal heat and vapor transfer coefficients are shown in Fig. 2.5.2 (Stage, 1983a, Fig. 10). The solutions are for the dry boundary layer. In this figure, the analytic solutions show that the horizontal heat (g_1) and vapor (g_2) transfer coefficients are 2.0 near the shore and eventually approach zero when fetch (x) approaches inifinity.

In order to evaluate the quality of the numerical solutions, they are compared with the analytical results. The numerical model has been run in both the wet (cloud formed) and the dry (no cloud formed) boundary cases, as shown in Fig. 2.5.3. The wet boundary layer case better resembles the real atmospheric situation. However, the result of the dry boundary layer case of the numerical solution is used to compare with the horizontal transfer coefficient solution which was analytically solved under the dry boundary layer condition.

The so called numerical dry (cloud-off) case is an artificial situation, which was obtained by applying the dry (cloud-free) boundary equation. This equation forcibly suppresses the radiation and latent heat release terms when saturation is encountered.

From the comparisons between the following two figures, Fig. 2.5.2 and Fig.2.5.3, it is clearly seen that

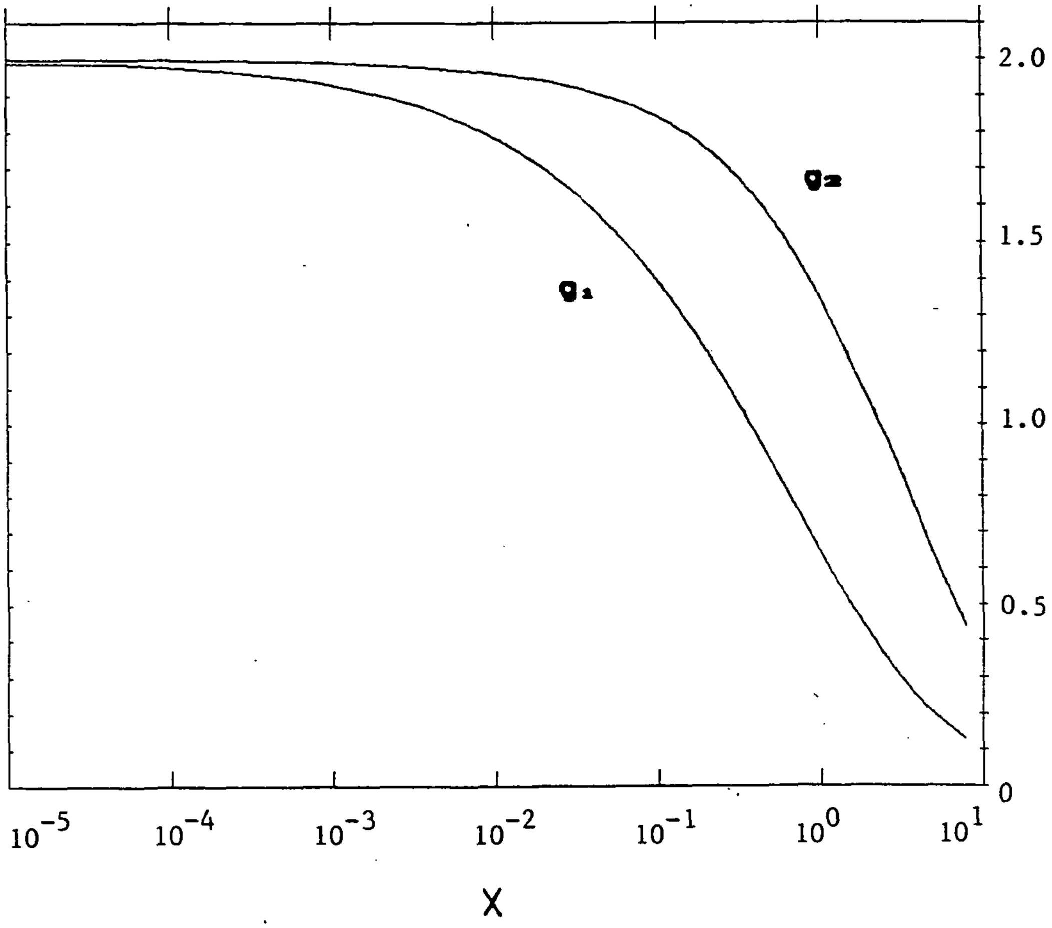

Fig.2.5.2 The analytical solutions for the dry MABL horizontal heat and vapor transfer coefficients.

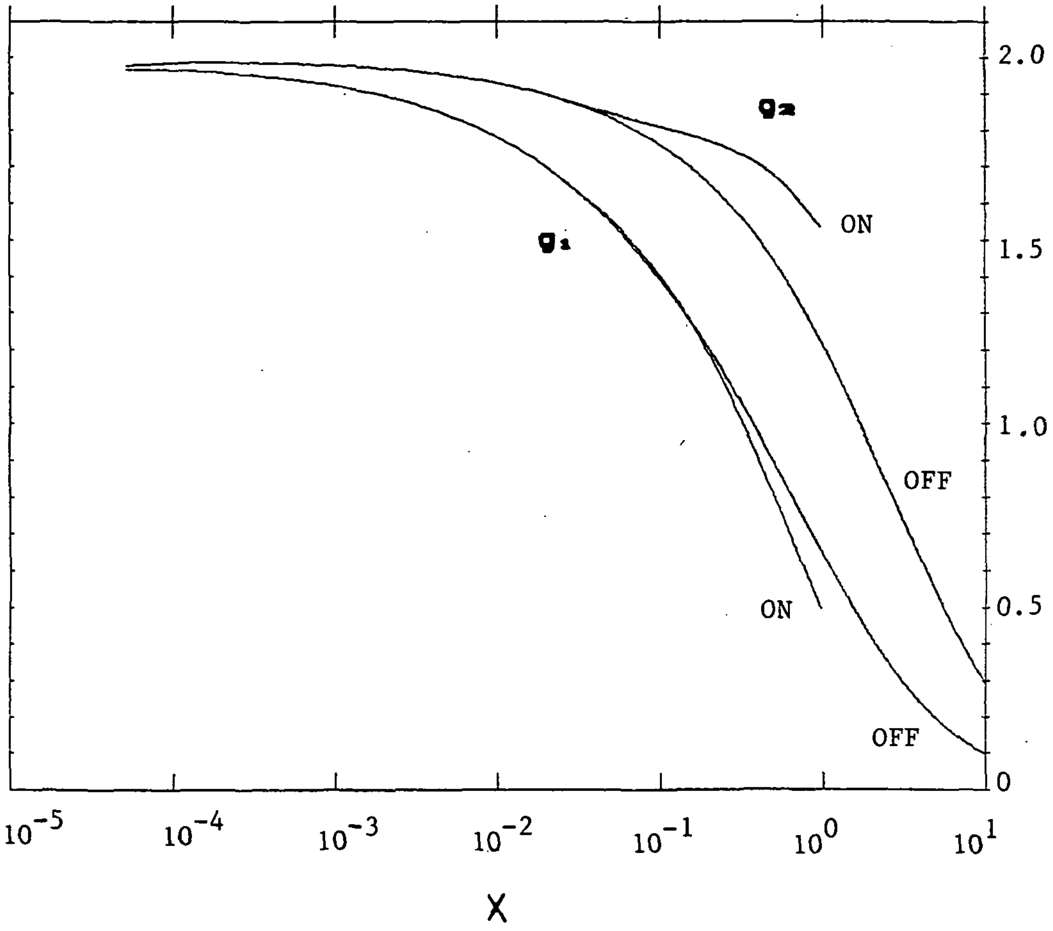

Fig.2.5.3 The numerical solutions for both the dry and wet MABL horizontal heat and vapor transfer coefficients.

the analytic solution, and the cloud free numerical solution of the horizontal heat and vapor transfer coefficients are identical at all fetches. This is theorectically accurate. Meanwhile, several conclusion can be made from these two figures, g_1 and g_2 as function of Log X.

First, it can be inferred that once clouds form the entrainment rate increases due to radiation and latent heat release in the cloud layer, then the boundary layer begins dry out due to increased entrainment of dry air from above (Stage 1979, Fig. 5.2.7). Therefore, once clouds form the boudary layer becomes drier than the cloud-off case at that same fetch. This will tend to increase the surface vapor fluxes and cause a large value of the horizontal vapor transfer coefficient for the cloud-on case. Also, the differences between the vapor transfer coefficients of the two cases increase following the boundary layer evolution. On the contrary, the horizontal heat transfer coefficient is larger for the cloud off case. It can be inferred too that once clouds form the boundary layer is more strongly heated by entrainment and is therefore warmer at any given fetch than the cloud-off case (Stage 1979, Fig. 5.2.8). This will tend to decrease the surface heat fluxes and cause a smaller value of the horizontal heat transfer coefficient.

Another noticeable point is that the analytical solutions start from zero fetch (x=0), i.e. Log X equals negative infinity. The numerical model sets up the initial condition of Z_{mI} = 30m, with the corresponding value of Log X ≅ -4.5. This assumption will be proven to be as good as a very thin boundary initial condition, eg: Z_{mI} = 0.1 m, by using the modified computation of model initial condition in the next chapter, sec. 3.2. The advantage of this assumption is that it saves a lot of computation time during the model's initial stage.

After all, it can be concluded that in the cloud-free regions the numerical solutions of horizontal transfer coefficients are equivalent to the analytical solutions derived by Stage (1983a).

However, the biggest advantage of the numerical method is that it is good not only for the dry boundary layer, but it also provides a means of computing the horizontal transfer coefficients for the wet boundary layer evolution case, as has been shown in Fig. 2.5.3. Thus, this result can be used as a relatively accurate forecast estimates of surface heat and vapor fluxes from shore into the cloud-topped regions during cold-air outbreaks of marine boundary layer evolution.

By comparing this section and last one, it is seen that the horizontal transfer coefficient method for the boundary layer heat and vapor fluxes can be independently solved either numerically or analytically, as shown schematically in Fig.2.5.4.

In the next chapter, further studies of how the transfer coefficients respond to the variations of the fundamental parameters will be discussed in details. A modified technique of computing the heat and vapor fluxes into the cloud-topped boundary layer during cold air outbreaks is also developed in the following sections.

2.6 Specification of The Model

In the last section, the extended numerical version of Stage and Businger's boundary layer model (1981a,b) has been shown to be identical to the analytical solutions to the cloud edge. In next chapter, the model will be run to simulate evolution of the surface heat and vapor fluxes from shore into the cloud-topped regions. Those runs are done under wide ranges of change of the boundary layer fundamental parameters. The ranges of values have been chosen corresponding to the greatest uncertainty range of measured data likely to be encountered in the real atmosphere. Thus, the results of these runs could be applied to the boundary layer evolution during most cold air outbreaks.

This modified numerical model is formed under the assumption of linear shoreline sounding profiles in order to simplify the problem. Thus, the fundamental dependent variables θ_m and q_T of the boundary layer at the shore may be specified by the sounding values at the shoreline surface θ_{m1}, q_{T1} and the lapse rates $\Gamma_{\theta m}$, Γ_{qT}. Alternatively, the shoreline soundings could be specified in terms of linear θ_1 and RH_1 (i.e. in terms of θ_{11}, RH_1, and the lapse rates $\Gamma_{\theta 1}$, Γ_{RH}). Other initial values of variables are $Z_m = Z_D = 0$, because we assume that $Z_B = Z_m + Z_D = 0$, and $Z_B = Z_m$ at the shore.

Altogether, the full set of external parameters during a cold-air outbreak episode are θ_{m1}, q_{T1}, $\Gamma_{\theta m}$, Γ_{qT} or θ_1, RH_1, $\Gamma_{\theta 1}$, Γ_{RH} which describe the shoreline sounding; wind speed (U); sea surface temperature (T_o); radiative sky temperature (T_{SKY}), or cloud top radiation cooling rate (R_B), and divergence (D_1 and D_2).

Thus, there are a total of 9 external parameters which are important to the evolution of the horizontal heat and vapor transfer coefficients during cold air outbreaks.

2.7 Modification of Model Initialization

The numerical model of simulating marine boundary layer evolution during cold outbreaks was first developed by Stage (1979). This model uses the assumptions of linear shoreline soundings as given in (2.4.1) and (2.4.2) and sets the initial values of fundamental variables as:

$$\left.\begin{aligned} Z_{BI} &= 0, \\ \theta_{MI} &= \theta_{M1}, \\ q_{TI} &= q_{T1}. \end{aligned}\right\} \quad \text{at } x = 0 \qquad (2.7.1)$$

θ_M and q_T are functions of Z_B, which become independent of the initial conditions rapidly (Stage, 1983a).

Stage (1979, 1983b) and Stage and Businger (1981a,b), were able to avoid spending large amounts of computation on the uninteresting and physically unrealistic initial growth of the boundary layer. They began their computation with

$$\left.\begin{aligned} Z_{BI} &= 30\ \text{m}, \\ \theta_{MI} &= \theta_{M,B+} - 0.001; \\ q_{TI} &= q_{T,B+}. \end{aligned}\right\} \quad \text{at } x = 0 \qquad (2.7.2)$$

This technique was appropriate for their computation purpose. However, it can be seen from (2.3.1) and (2.3.2) that the net sensible (H) and latent (H_L) heat input to the boundary layer have different values for (2.7.1) and (2.7.2). For previous studies the difference is slight. Nevertheless, evolutions of H and H_L are the main topics of this paper, therefore a more accurate model initialization to estimate H and H_L is required here.

The modified initialization method is based on the analytical solution (Stage, 1983a), and begins the numerical model computations at the fetch where the dry MABL was grown from the linear soundings of θ_e and q_T at the shore to Z_B equal to 30 m. The net sensible (F_{SENS}) and latent heat (F_{LAT}) fluxes input are computed by the following steps.

$$Z_{BI} = 30 \text{ m}$$

$$\theta_{eI} = \theta_{e,B+}$$

$$q_{TI} = q_{T,B+} \qquad (2.7.3)$$

$$\theta_{lI} = \theta_{l,B+} = \theta_{e,B+} - (L/C_P)q_{T,B+}$$

Assuming $\theta_l \cong \theta_v$ ($\because q_l \cong 0$), from Stage (1983)

$$\theta_1 = \theta_{11} + \frac{1+A}{1+2A} (\theta_{1,B+} - \theta_{11}) \qquad (2.7.4)$$

Then, F_{SENS} and F_{LAT} can be approximated by θ_1.

$$F_{SENS} = (\theta_1 - \frac{1}{2} (\theta_{11} + \theta_{1,B+})) Z_B \qquad (2.7.5)$$

$$F_{LAT} = \frac{L}{C_p} F_{SENS} \left(\frac{q_0 - q_{T,1}}{\theta_0 - \theta_{l,1}} \right) \qquad (2.7.6)$$

Because $\theta_1 \cong \theta$, by using

$$\theta_v = (1 + (1/\epsilon - 1) q_{T1}) \theta_1 \qquad (2.7.7)$$

and bulk transfer formula, surface sensible heat flux, $\overline{W'\theta_v'}|_0$, can be computed. Then, the estimated time and fetch are obtained as:

$$t = F_{SENS} / \overline{W'\theta_v'}|_0 , \qquad (2.7.8)$$

$$x = U t . \qquad (2.7.9)$$

Also, the potential temperature and mixing ratio of the boundary layer are estimated as:

$$q_T = \frac{1}{2} (q_{T,B+} + q_{T1}) + \frac{F_{LAT}}{\frac{L}{C_p} Z_B} , \qquad (2.7.10)$$

$$\theta_w = \theta_1 + \frac{L}{C_p} q_T \, . \qquad (2.7.11)$$

A further study of the horizontal tranfer coefficients, from (2.4.3) to (2.4.7), and the bulk transfer formulas, the initial values of g_1 and g_2 can be derived.

$$g_1 = \frac{2}{C_{T1}(\theta_{v0}-\theta_{v1})X} \left(H_v / \rho C_P \right)$$

$$= \frac{2}{C_{T1}(\theta_{v0}-\theta_{v1})X} F_{SENS}$$

$$= \frac{2}{C_{T1}(\theta_{v0}-\theta_{v1})X} C_T U(\theta_{10}-\theta_{11})t \cong 2.0 \qquad (2.7.12)$$

$$g_2 = \frac{2}{C_{T1}\frac{L}{C_p}(q_0-q_1)X} \left(H_L / \rho L \right)$$

$$= \frac{2}{C_{T1}\frac{L}{C_p}(q_0-q_1)X} F_{LAT}$$

$$= \frac{2}{C_{T1}\frac{L}{C_p}(q_0-q_1)X} C_q U(q_0-q_{T1})t(L/C_P) \cong 2.0 \qquad (2.7.13)$$

it is assumed that $C_T = C_q$ and $C_T = C_{T1}$ during the initial stage.

This modified approximation of F_{SENS} and F_{LAT} during the initial stage of MABL evolution provides an explicit set of equations for model calculations and introduces only a very small errors.

Meanwhile, it has also been proven that the initial analytical values of the horizontal transfer coefficients are approximated to be 2.0.

It will be seen later in figures of Sec.3.1 that the initial values of g_1 and g_2 of the numerical solution are almost identical to the analytical solutions derived here. This is another proof of the credibility of this modified numerical marine atmospheric boundary layer model.

2.8 Modification of the Model Time Step

This model uses a variable time step, DT. The time step depends on how rapidly the mixed layer evolves and is defined as :

$$DT = \mathrm{MIN}\left(\frac{dz_{max}}{W_e+|W_l|}, \left|\frac{d\theta_{max}}{d\theta_e/dt}\right|, \left|\frac{dq_{max}}{dq_T/dt}\right|, \frac{z_B \cdot fraction}{W_e+|W_l|}\right) \tag{2.8.1}$$

where the default values of the parameters set up in this model are: dZmax = 20M; dθmax = 0.05; dqmax = 0.05×10^{-3} and fractional change of Z_B = $0.05 \times Z_B$. These constants limit the maximum changes in Z_B, θ_e, q_T and the fractional change of Z_B which are allowed in any one time step of the model run.

In general, the boundary layer grows rapidly during the initial stage, so DT is small. Then, as time goes on the layer growth rate will decrease, and DT becomes larger and larger. If we use DT given by (2.8.1), trouble occurs for very long fetches, because DT is so large that the changes in θ_e and q_T in a single time step become too large as a fraction of the air-sea differences in θ_e and q_T. Meanwhile, the characteristics of the boundary layer evolution will be lost too.

In the extended version of this numerical model, additional limits on the size of the time step, DT, are imposed. In addition to satisfying (2.8.1), DT is limited by

$$DT \leq 0.1 \left| \frac{\theta_{eo} - \theta_e}{d\theta_e/dt} \right| \tag{2.8.2}$$

$$DT \leq 0.1 \left| \frac{q_{To} - q_T}{dq_T/dt} \right| \tag{2.8.3}$$

These conditions guarantee that $\theta_{eo} - \theta_e$ and $q_{To} - q_T$ do not change by more than 10% in any one time step.

2.9 Specification of Model Termination

In addition, we put condition checks into the new version of numerical model in order terminate the runs before physically unrealistic cases develop. These termination factors of the boundary layer evolution are shown and briefly explained in Table 2.9.1.

Table 2.9.1

The terminating factors of the MABL model.

Terminating factors	Physical reasons
1. $Z_B > 5000$ m	When Z_B becomes more than 5km, it is far beyond the normal BL height of 1-2 km. The well mixed boundary layer assumption can not be expected to hold for such large boundary layer depth.
2. $Z_B < 30$ m	Z_B has been unrealistically suppressed by divergence.
3. $Z_C < 0$ m	This study does not include cases of stratus fogs.
4. $T_{SKY} < -273$°C	The radiative sky temperature must be above 0 K.
5. $R_B < 0$ W/m^2	This study does not include cases of cloud top radiation warming during cold air outbreaks.
6. $X_3 < 0$	Free entrainment cases are not included in this study.

7. $DTHV < 0$	Cases of encroachment are not included in this study.

CHAPTER 3 MODEL RESPONSES TO VARIATION OF EXTERNAL PARAMETERS

3.1 The Responses of Horizontal Transfer Coefficients to The Variation of External Parameters

Stage (1983b) has studied the evolution of basic thermodynamic variables of the marine boundary layer during cold air outbreaks. He pointed out how these factors were influenced by the variation of external parameters. This study will concentrate on how much these parameters influence the evolution of horizontal heat and vapor transfer coefficients.

In this section, all the test runs are based on the New York sounding profile which has been studied by Stage and Businger (1981b), Chou and Atlas (1982), Stage (1983a,b). This sounding is considered to be a typical air modification profile of cold-air outbreaks and is used to demonstrate the importance of various physical processes in determining boundary layer evolution. This sounding is shown in Table 3.1.1.

In this section tests are run by varing each of the

Table 3.1.1

Parameters of the basic test case (based on New York sounding, Feburary 1979)

Water Surface		
Temperature	T_O	$= 12^\circ C$
Mixing Ratio	q_O	$= Q_{SAT}(T_O) = 8.6 g/kg$
Wind speed	U	$= 15 m/sec$
Divergence	$\vec{\nabla} \cdot \vec{U}$	$= 0 /sec$
Radiative Sky Temperature	T_{SKY}	$= -40^\circ C$
Potential Temperature Sounding	θ	$= 3.0^\circ C + 3.8^\circ C/km\ Z$
Total Water Mixing Ratio Sounding	q_T	$= 3.4 g/kg - 0.75 g/kg/km\ Z$

external parameters one at a time, and noting the resulting responses of the horizontal transfer coefficients.

A. Wind Speed

The test runs of wind speed varing from 1, 2, 4, 8, 16 to 32 m/sec with the responses of g_1 and g_2 are shown in Fig.3.1.1.

As noted by Stage (1983a), wind speed has no effect on the distance required for cloud formation nor on the layer evolution before cloud forms. Low wind cases require a longer time to reach a given fetch, and cause smaller surface sensible and total water vapor fluxes, so that the radiation terms are dominant in the cloud regions for the low wind cases. In high wind cases, radiation is then relatively less dominant than surface fluxes. From (2.4.3), (2.4.4), (2.4.5) and the bulk transfer formulas:

$$\overline{W'\theta_v'}|_o = C_T U(\theta_{vo} - \overline{\theta}_v),$$

(3.1.1)

$$\overline{W'q_T'}|_o = C_q U(q_{To} - \overline{q}_T).$$

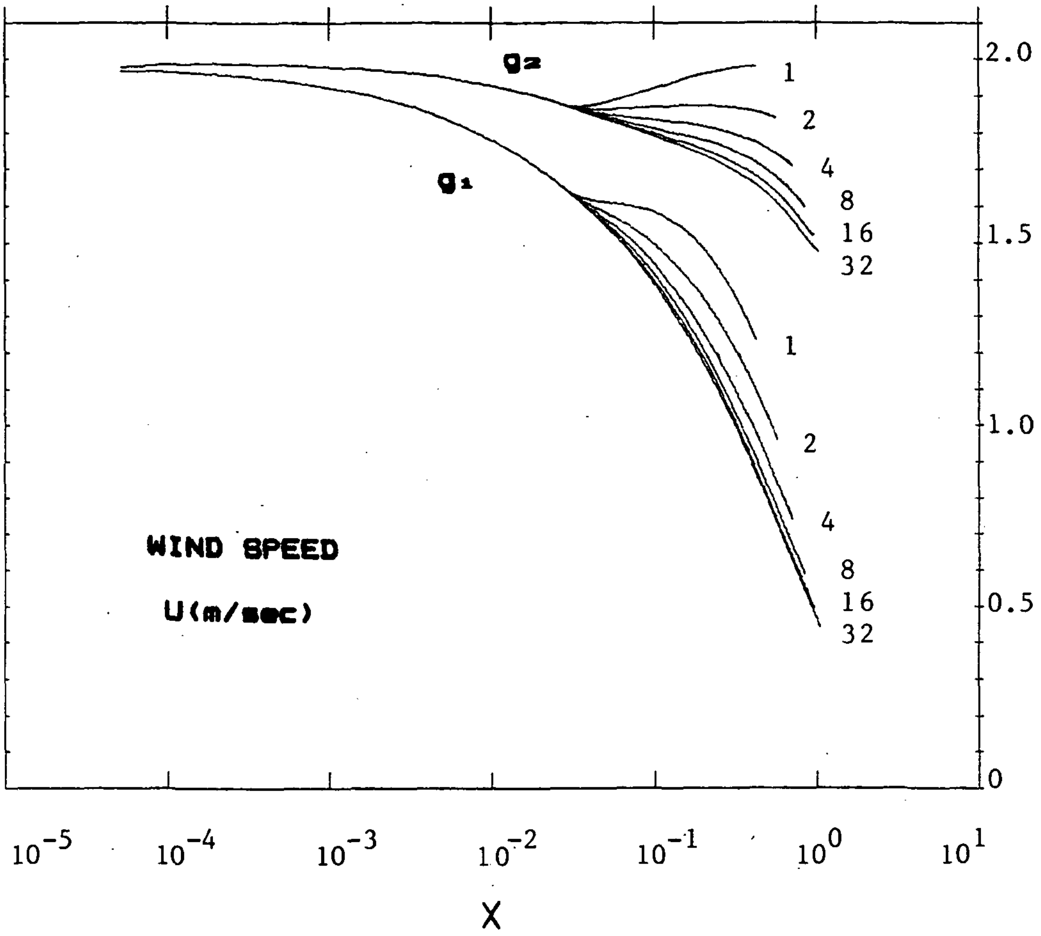

Fig.3.1.1 g_1 and g_2 as functions of X for various wind speed. (U: 1 to 32 m/sec)

It can be shown that

$$g_1 \infty \frac{H_v}{x} \infty \frac{\rho C_p}{x} \int_0^x C_T(\theta_{vo} - \bar{\theta}_v)dx,$$

$$g_2 \infty \frac{H_L}{x} \infty \frac{\rho L}{x} \int_0^x C_q(q_{To} - \bar{q}_T)dx, \tag{3.1.2}$$

and it is seen that g_1 and g_2 do not directly depend on wind speed in the dry case provided that C_T and C_q are not functions of wind speed (see discussions in Stage 1983a). However, from Fig. 3.1.1 it is seen that wind speed has little effect on g_1 and g_2 for the high wind speed (surface heat fluxes dominant) cases. For the low wind speed (radiation dominant) cases, although cloud top radiation cooling and surface heat fluxes input partly offset each other , g_1 and g_2 values are larger than those for higher wind speed. Also, the changes of g_1 and g_2 are much larger when wind speed are smaller, this suggetsts that wind speed has indirect effect on g_1 and g_2.

One important note is that with a large variation of wind speed ranging from 1 m/sec to 32 m/sec, the model predicted values of horizontal transfer coefficients g_1 and g_2 have less than 32% variation at any given fetch up to LOG X = 0 (i.e. fetch ≅ 1900 km). In general g_2 is less dependent on wind speed than g_1, and more details are shown in Table 3.1.2.

B. Divergence

Two different types of divergence D_1 and D_2 are included. They were first defined in Stage (1983a). D_1 is the divergence confined in and resulting from the boundary layer. Changes of surface roughness and fluxes or the baroclinicity in the boundary layer are all possible causes of D_1, and are assumed to act only up to Z_B. Since this numerical model assumes a sufficiently convective boundary layer, the layer can be treated as a well mixed slab, D_1 can be assumed independent of height. D_2 is the synoptic scale divergence which is assumed to be uniform at all levels of interest, because the levels which are interested by our boundary layer studies are much less than the scale height for the synoptic weather patterns.

The series of D_1 and D_2 runs in this section are done by setting cloud top radiation cooling rate (R_B) constant at 0.1 mK/sec (i.e. 128 W/m^2).

First, let D_1 = -10×10^{-6} to 10×10^{-6} sec^{-1}, in increments of 2×10^{-6} sec^{-1}, and $D_2 = 0$; i.e. from large convergence cases to divergence free and finally to large

Table 3.1.2

The changes of g_1 and g_2 caused by a 32-fold change in wind speed. U : 1 - 32 m/sec.

LogX	x (km)	Range of U m/sec	Range of g_1 ($\bar{g}_1 \pm \Delta g_1$)	 g_2 ($\bar{g}_2 \pm \Delta g_2$)	Percent change in g_1 ($2\Delta g_1/\bar{g}_1$)	 g_2 ($2\Delta g_2/\bar{g}_2$)
-1.0	193	1 to 32	1.49 ± 0.11	1.85 ± 0.06	14.0%	6.7%
-0.5	611	1 to 32	1.19 ± 0.19	1.83 ± 0.15	31.6%	15.9%
0.0	1932	8 to 32	0.67 ± 0.08	1.63 ± 0.08	21.9%	8.9%

divergence cases. The responses of g_1 and g_2 are shown in Fig. 3.1.2a.

It is clearly shown from this figure that for any given fetch g_1 and g_2 differ by less than 55% of their range when D_1 is changed. The uncertainty of heat transfer coefficient g_1 is more than that of the mixing ratio transfer coefficient g_2. It is also computed that the values of g_1 change less than 55% for the range of D_1 values tested, and g_2 changes less than than 36%. More details are shown in Table 3.1.3a.

The top of boundary layer is pushed upward by convergence and pulled downward by divergence, thus cloud can be formed at shorter fetches with larger convergence and suppressed with divergence. This is shown in Fig. 3.1.2b. For $D_1 > 4\times10^{-6}$ $\sec^{-1}$, no curves are shown in Fig. 3.1.2b, because a cloud can not be formed under such large divergence.

Since the boundary layer becomes thinner with increased divergence, the mixed layer potential temperature θ_m, and total water mixing ratio q_T are higher, which has been shown by Stage (1983a, Fig. 8, and 1983b Fig. 10). The effects of large divergence will increase the average θ_m and q_T of the boundary layer, although it is partially offset by the entrained cold and dry air from above cloud top , the surface heat and vapor

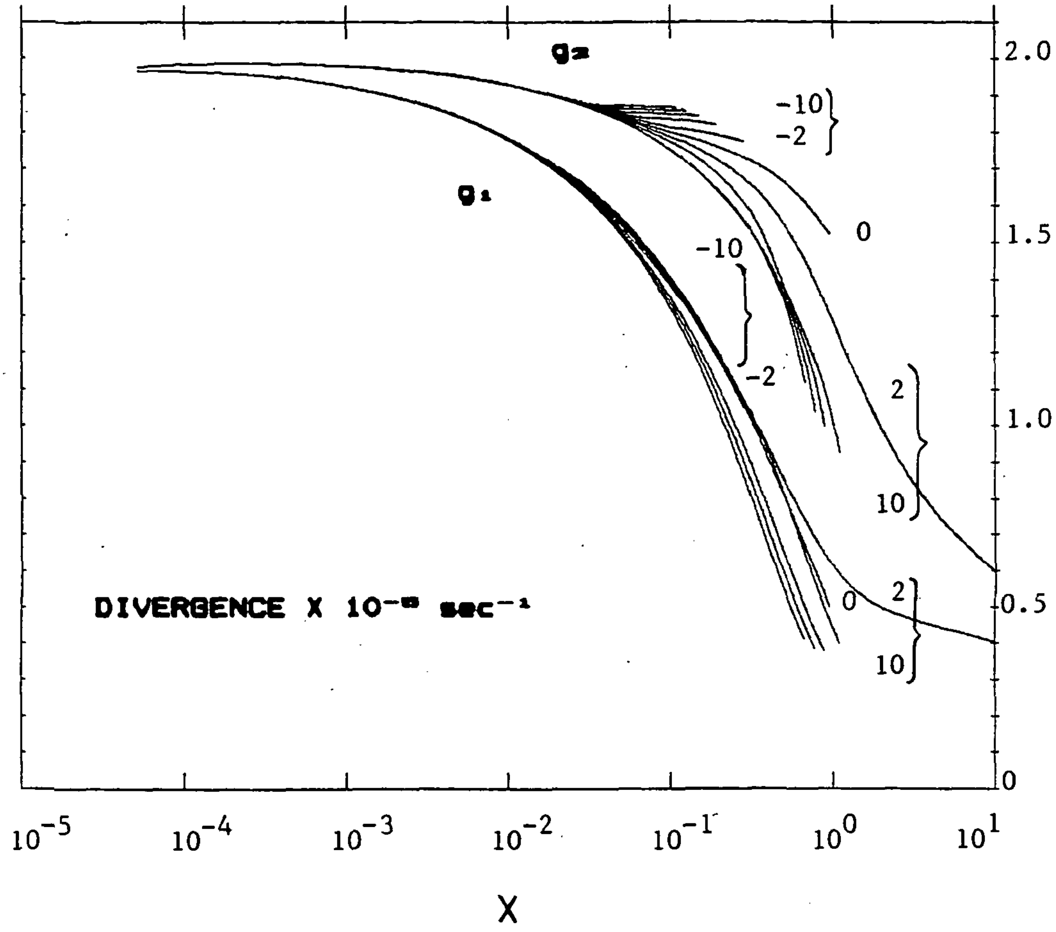

Fig.3.1.2a g_1 and g_2 as functions of X for D_1 type divergence changes. (D_1: -10 to 10×10^{-8} $\sec^{-1}$)

Table 3.1.3a

The changes of g_1 and g_2 caused by D_1 type divergence. D_1 changes from -10×10^{-5} to 10×10^{-5} sec^{-1}, in increments of 2×10^{-5} sec^{-1}, and $D_2 = 0$.

LogX	x (km)	Range of D_1 ($10^{-5}sec^{-1}$)	Range of g_1 ($\bar{g}_1 \pm \Delta g_1$)	Range of g_2 ($\bar{g}_2 \pm \Delta g_2$)	Percent change in g_1 ($2\Delta g_1/\bar{g}_1$)	Percent change in g_2 ($2\Delta g_2/\bar{g}_2$)
-1.0	193	-10 to +10	1.35±0.04	1.81±0.06	6.2%	6.9%
-0.5	611	- 2 to +10	0.93±0.12	1.65±0.11	24.7%	13.8%
0.0	1932	+ 4 to + 6	0.57±0.16	1.35±0.24	54.5%	35.4%

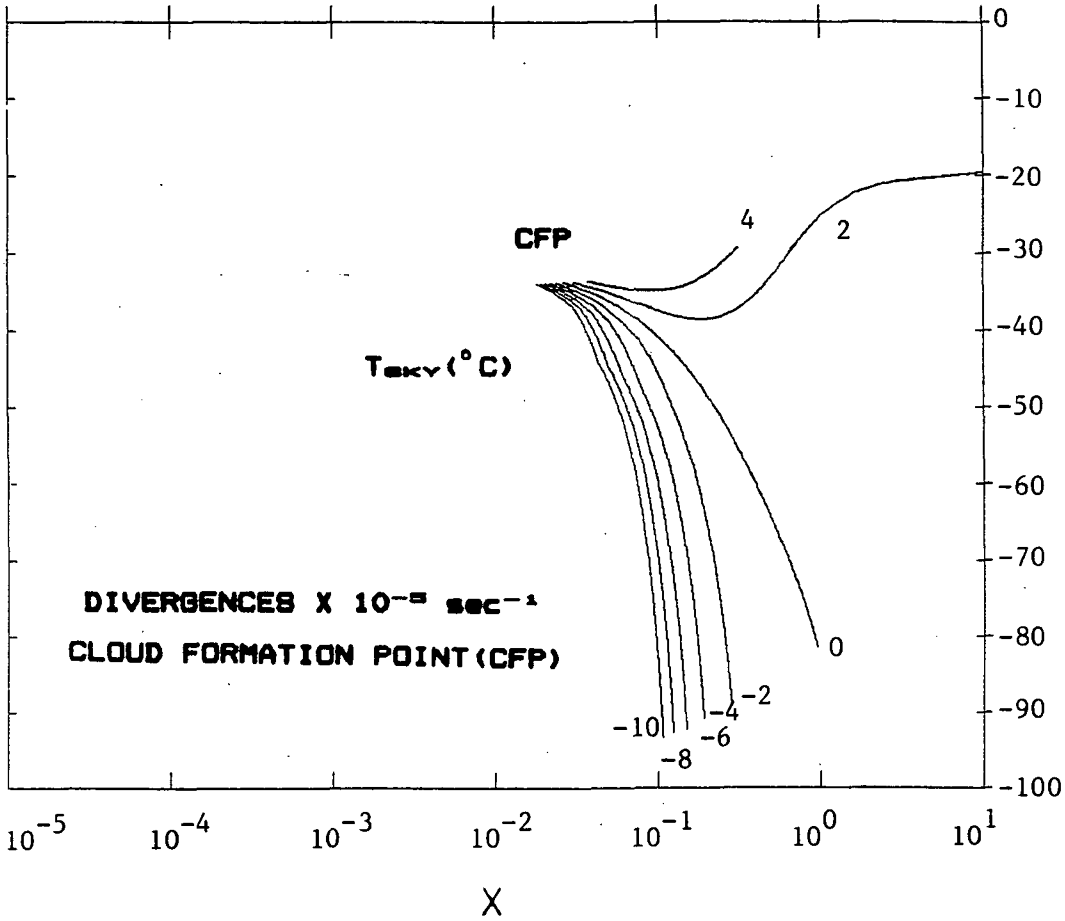

Fig.3.1.2b T_{SKY} as function of X for D_1 type divergence changes. (D_1: -10 to 10×10^{-5} sec^{-1})

fluxes tend to decrease with the increased average potential temperature and mixing ratio of boundary layer. It is clearly seen on Fig. 3.1.2a that the horizontal transfer coefficients are smaller for larger divergences.

Next, the effects of D_2 variation on g_1, g_2 and T_{SKY} with constant R_B at 0.1 mK/sec are shown in Fig. 3.1.3a and Fig. 3.1.3b respectively. During these test runs, $D_2 = -10\times10^{-6}$ to 10×10^{-6} sec^{-1}, in increments of 2×10^{-6} sec^{-1}, and $D_1 = 0$.

The variations in g_1 and g_2 respond to changes in D_2 can be understood by using explanations used for D_1. The ranges of variation in g_1 and g_2 due to the change of D_2 are less than 32% of the average values at any given fetch. The changes in g_1 are smaller than that of g_2 for the range of D_2 values tested. It is also noticed that the changes in g_1 and g_2 will tend to increase with increased fetch. Further details are discussed in Table 3.1.3b as shown in the following page.

In Fig. 3.1.3b, it is seen that the cloud is formed at a shorter fetch with stronger convergent motions. For D_2 larger than 4×10^{-6} sec^{-1}, no curves are shown in Fig. 3.1.3b, because cloud can not be formed under suppression by such strong downward motion.

From the conclusion above, we learn that basically the changes of D_1 and D_2 have similar effects on g_1 and

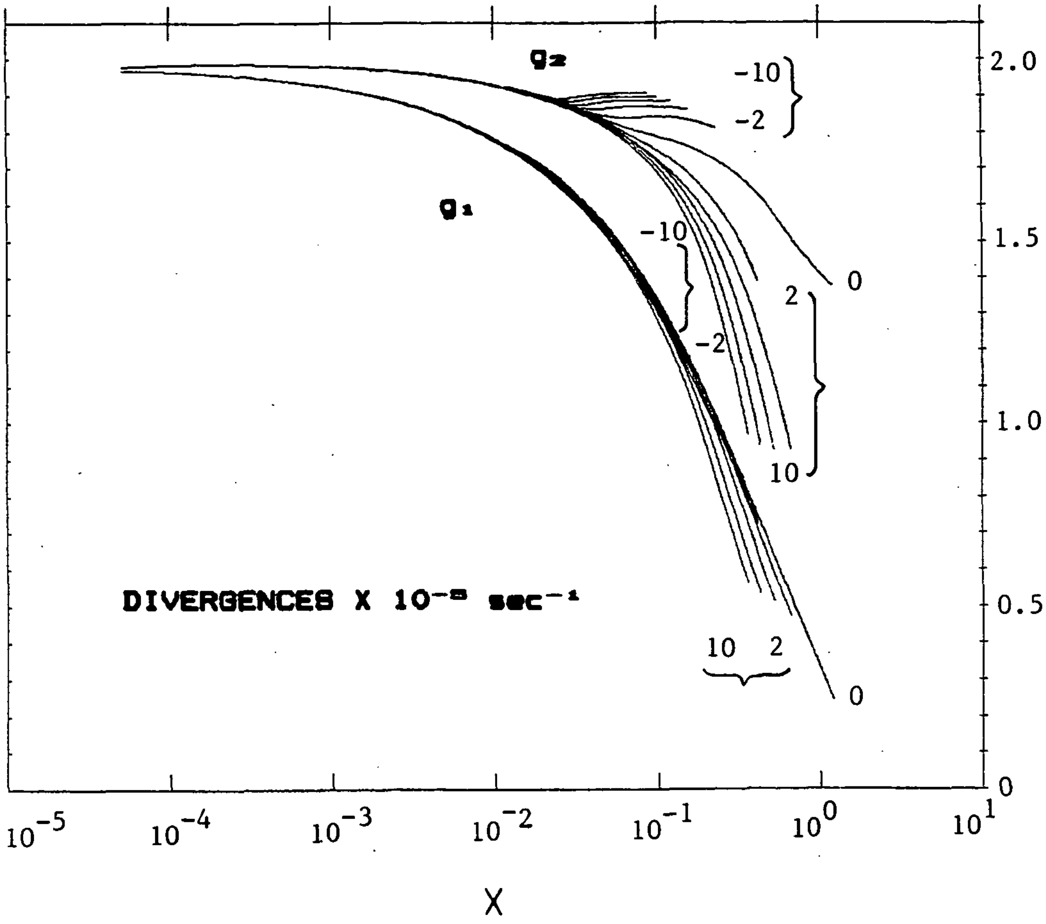

Fig.3.1.3a g_1 and g_2 as functions of X for D_2 type divergence changes. (D_2: -10 to 10×10^{-6} sec^{-1})

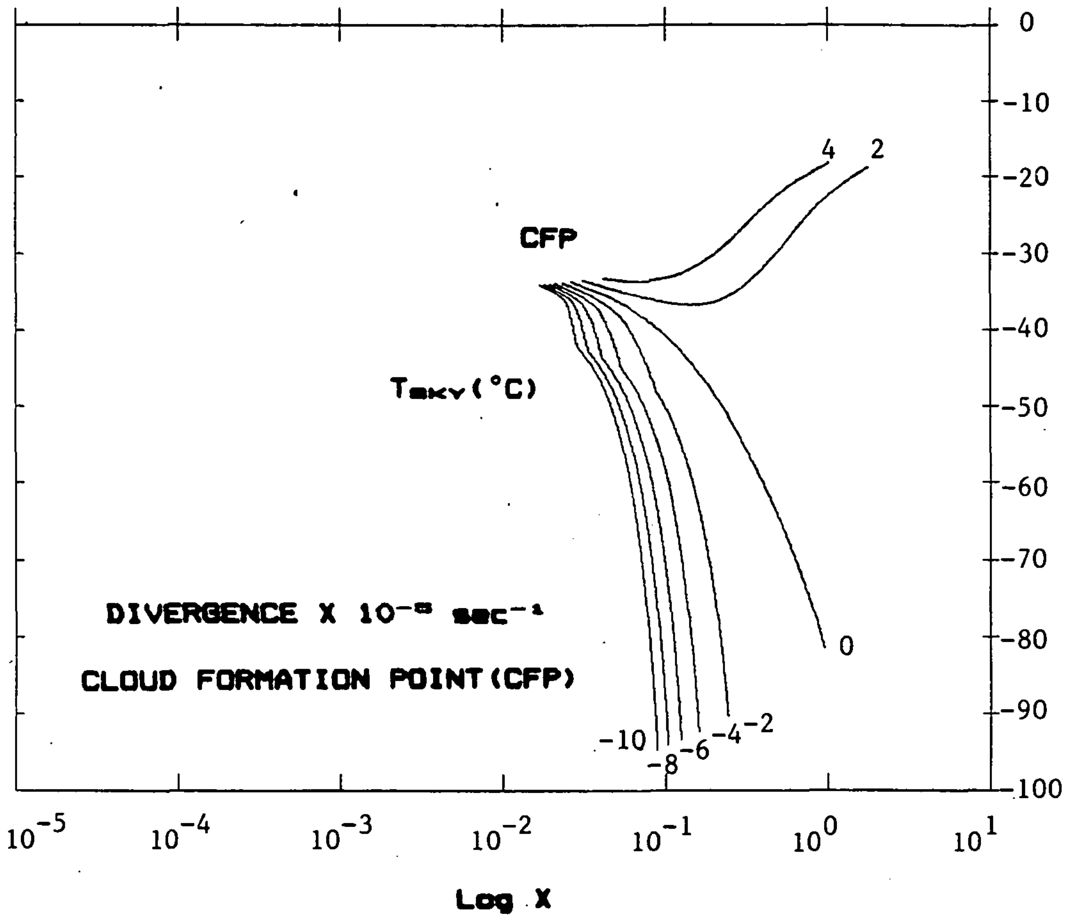

Fig.3.1.3b T_{sky} as function of X for D_2 type divergence changes. (D_2: -10 to 10x10^{-6} sec^{-1})

Table 3.1.3b

The changes of g_1 and g_2 caused by D_2 type divergence. D_2 changes from -10×10^{-8} to 10×10^{-8} sec^{-1}, in increments of 2×10^{-8} sec^{-1} and $D_1 = 0$.

LogX	x	Range of	Range of		Percent change in	
		D_2	g_1	g_2	g_1	g_2
	(km)	($10^{-8}\mathrm{sec}^{-1}$)	($\bar{g}_1 \pm \Delta g_1$)	($\bar{g}_2 \pm \Delta g_2$)	($2\Delta g_1/\bar{g}_1$)	($2\Delta g_2/\bar{g}_2$)
-1.0	193	-10 to +10	1.31±0.03	1.80±0.11	4.3%	12.6%
-0.5	611	+ 2 to +10	0.75±0.10	1.31±0.21	25.6%	31.9%
-0.37	824	+ 4 to + 8	0.63±0.08	1.30±0.16	24.2%	25.0%

g_2. However, g_1 and g_2 do have a wider range of responses with respect to changes in the synoptic scale type divergence (D_2). Also, by comparing the values of g_1 and g_2 at any given fetch for the same value of D_1 or D_2, it is noticed that D_2 does have a stronger suppression on the vapor and heat fluxes input to the boundary layer as shown in Table 3.1.3a and 3.1.3b.

C. Sea Surface Temperature (T_o)

Test runs were done with T_o = 6, 8, 10, 12, 14, 16 and 18 °C, as shown in Fig. 3.1.4. The resulting variations of g_1 and g_2 due to water surface temperature (T_o) change are in a range of about 5 to 35% of its value at any given fetch. g_2 is much less sensitive to the change of T_o than g_1 is. More details are shown in Table 3.1.4.

In Fig. 3.1.4, it is also seen that increasing T_o increases the surface heat fluxes, this tends to speed the growth , warming and moistening the boundary layer. Therefore, the boundary layer average temperature and mixing ratio will increase, which partially offset the increase of surface fluxes. This offset is larger for the heat fluxes, which can be seen in Fig. 3.1.4 that the

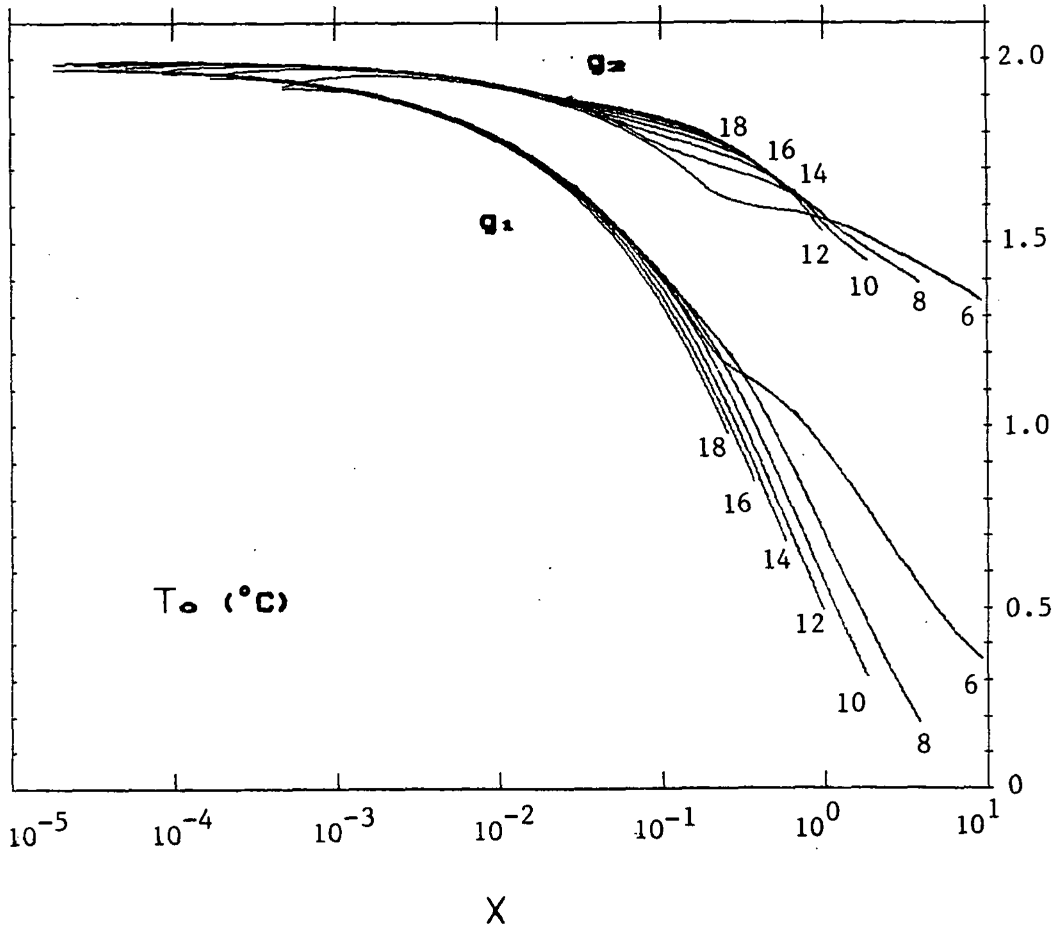

Fig.3.1.4 g_1 and g_2 as functions of X for various water surface temperature (T_o: 6 to 18°C).

Table 3.1.4

The changes of g_1 and g_2 caused by a change in water surface temperature, T_o. T_o: 6 to 18°C, in increments of 2°C.

Log X	x	Range of	Range of		Percent change in	
		T_o	g_1	g_2	g_1	g_2
	(km)	(°C)	($\bar{g}_1 \pm \Delta g_1$)	($\bar{g}_2 \pm \Delta g_2$)	($2\Delta g_1/\bar{g}_1$)	($2\Delta g_2/\bar{g}_2$)
-1.0	81-292	6 to 18	1.38±0.05	1.80±0.05	7.0%	5.3%
-0.5	257-923	6 to 16	0.87±0.11	1.66±0.08	25.9%	9.6%
0.0	1210-1932	8 to 12	0.60±0.11	1.55±0.02	36.8%	2.1%

values of g_1 becomes smaller at large fetch for a warmer water surface temperature. The cases with cooler water surface temperature have weaker surface fluxes and are more strongly affected by the radiation after cloud formed. The cloud top radiation cooling decrease the average boundary layer temperature and mixing ratio, hence the surface fluxes input become larger for the colder water surface temperature after cloud formation point. This phenomenon becomes more significant especially at very large fetch. It is also seen from Fig. 3.1.4 that the nondimensional fetch (X) starts off at a smaller value with larger water surface temperature.

Another noticable feature is that sensible heat transfer coefficient g_1 decreases with increased T_o and partially offsets the sensible heat flux increase due to larger T_o. However, vapor transfer coefficient g_2 increases with increased T_o, and thus enhances the vapor heat flux effect.

D. Sky Temperature (T_{SKY})

Changing radiative sky temperature from 0, -20, -40, -60 to -80 °C is one way to study the boundary layer radiation cooling effects on the cloud top. The test runs are shown in Fig. 3.1.5. First, we noticed that for this

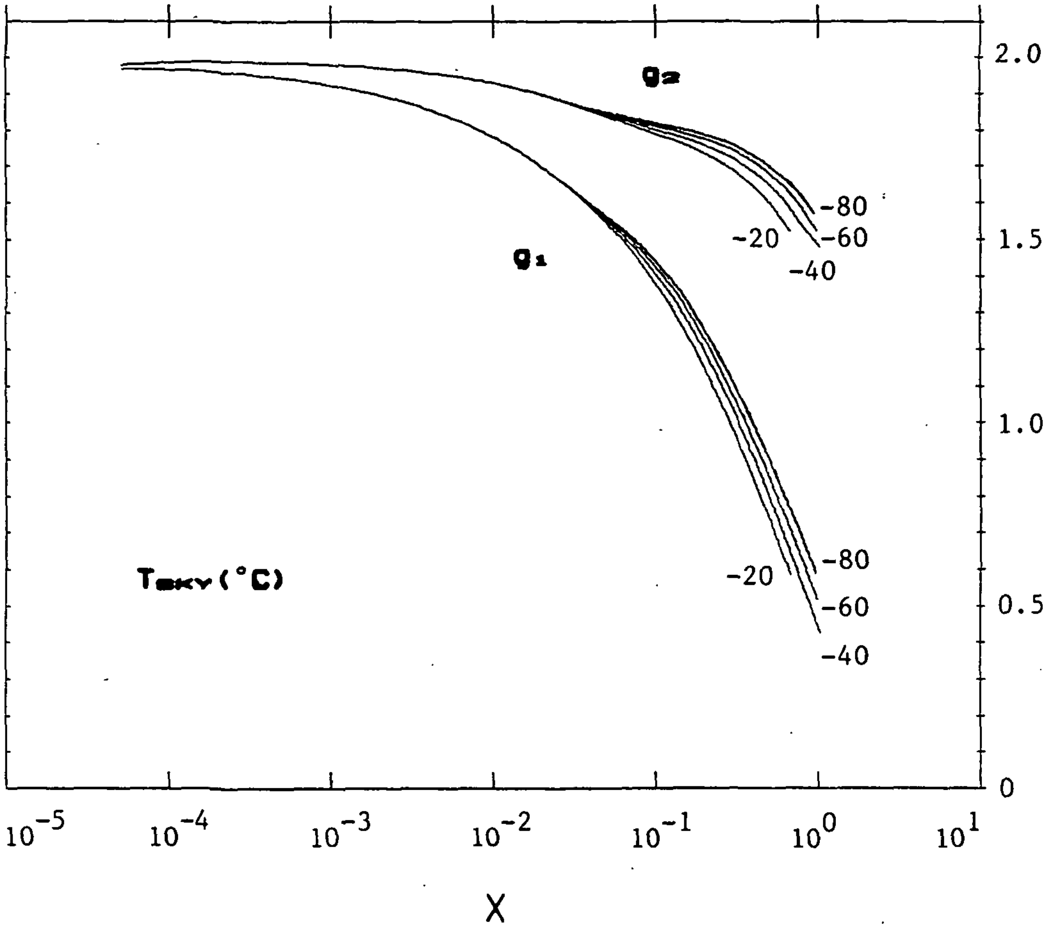

Fig.3.1.5 g_1 and g_2 as functions of X for various radiative sky temperature (T$_{sky}$: 0 to -80°C).

range of change of T_{SKY} the change of g_1 is between 5 to 25% of its average value, and the range of change of g_2 is even smaller between 2 to 5% of its average value at any given fetch. Further details are presented in Table 3.1.5.

Decreasing T_{SKY} increases the cloud top radiation cooling rate, R_B, so there is a larger entrainment rate and thicker cloud. The surface sensible and latent heat fluxes increase because of the decrease of average boundary layer potential temperature and total water mixing ratio, and they partially offset the radiation cooling effect. But, we can see from Fig. 3.1.5 that both heat and vapor horizontal transfer coefficients become larger with a smaller T_{SKY} temperature. This means that the surface heat and vapor fluxes increase dominates the effect of increased radiation cooling and the effect of entraining cold and dry air from above cloud top into boundary layer. Therefore, it can be concluded that decreasing T_{SKY} increases the cloud top radiation cooling, and it also speeds up the boundary layer growth.

These runs are terminated when T_{B+} becomes smaller than T_{SKY}, because this produces cloud top radiation warming, i.e. $R_B < 0$, which is considered physically unrealistic in cold-air outbreaks.

Table 3.1.5

The changes of g_1 and g_2 caused by T_{SKY}. T_{SKY}: 0 to -80°C, in increments of -20°C.

Log X	x (km)	Range of T_{SKY} (°C)	Range of		Percent Change in	
			g_1 ($\bar{g}_1\pm\Delta g_1$)	g_2 ($\bar{g}_2\pm\Delta g_2$)	g_1 ($2\Delta g_1/\bar{g}_1$)	g_2 ($2\Delta g_2/\bar{g}_2$)
-1.0	193	-20 to -80	1.43±0.03	1.80±0.02	4.4%	1.8%
-0.5	611	-20 to -80	1.03±0.07	1.72±0.04	13.8%	4.6%
0.0	1932	-20 to -80	0.51±0.06	1.53±0.04	25.0%	5.2%

E. Cloud Top Radiation Cooling (R_B) :

Another way to specify the cloud top radiation cooling effect is to use constant value of R_B through each run. R_B of 0., 0.05, 0.10, 0.15, 0.20, 0.25, 0.30 mK/sec were used in the test runs shown in Fig. 3.1.6. This corresponds to radiative heat fluxes from about 0 to 384 W/m^2 in increments of 64 W/m^2. The ranges of variation of g_1 and g_2 are still quite small for the range of change of R_B being tested. Ranges of both horizontal heat and vapor transfer coefficients increase with increased fetch. Among the two coefficients, g_2 is less sensitive to the variation of R_B than is g_1. Further details are shown in Table 3.1.6.

Similar to the discussions of test runs for T_{SKY}, it can be inferred that stronger cloud top radiation cooling can cause larger entrainment rate and speed up boundary layer growth. Therefore, when R_B = 0.25 and 0.30 mK/sec, Z_B exceeds 5km at very short fetch, and the run are terminated. This is seen on Fig. 3.1.6.

As has been shown in Fig. 3.5.2b and Fig. 3.5.3b, it can be easily seen that the variations of radiative sky temperature (T_{SKY}) were very large during boundary layer evolution while holding radiation cooling constant. So,

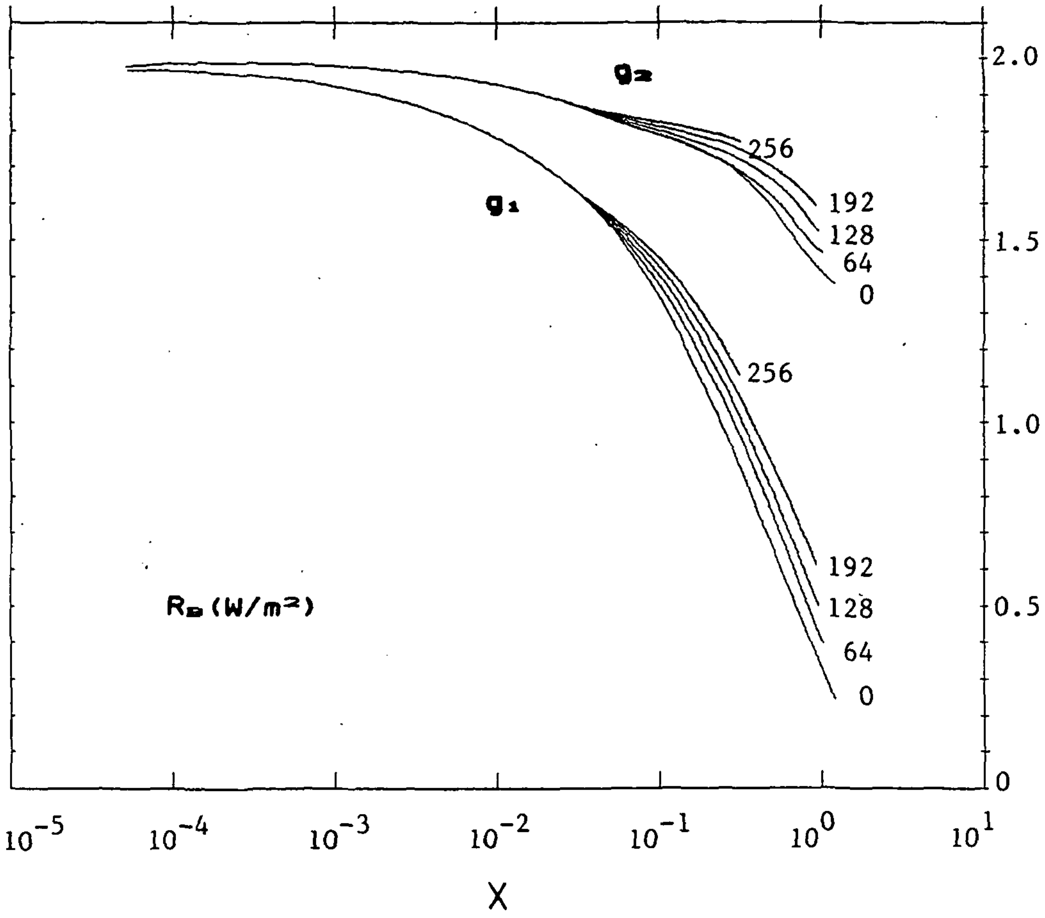

Fig.3.1.6 g_1 and g_2 as functions of X for various cloud-top radiation cooling rate (R_B: 0 to 256 W/m²).

Table 3.1.6.

The changes of g_1 and g_2 caused by R_B. R_B : 0.0 to 0.30 mK/sec, in increments of 0.05 mK/sec.

LogX	x (km)	Range of RB (W/m^2)	Range of g_1 ($\bar{g}_1 \pm \Delta g_1$)	Range of g_2 ($\bar{g}_2 \pm \Delta g_2$)	Percent Change in g_1 ($2\Delta g_1/\bar{g}_1$)	Percent Change in g_2 ($2\Delta g_2/\bar{g}_2$)
-1.0	193	0 to 256	1.39±0.06	1.80±0.02	8.0%	1.8%
-0.5	611	0 to 256	0.95±0.10	1.72±0.05	20.0%	5.6%
0.0	1932	0 to 128	0.33±0.08	1.46±0.06	47.6%	7.6%

holding T_{SKY} constant is not a good assumption.

However, physically holding cloud top radiation cooling (R_B) equal to constant is probably a better assumption than holding the radiative sky temperature constant as was done in the previous section. This concept can be easily explained. As the boundary layer evolves, the cloud top becomes higher and therefore colder. Meanwhile there is less water vapor above Z_B and the air above Z_B is colder, thus the radiative sky temperature also decreases. Since both the temperature at cloud top and the average radiative sky temperature above cloud top decrease, cloud top radiation cooling will remain relatively constant.

F. Initial linear shoreline sounding ($\theta_{e1}, \Gamma_{\theta e}; q_{T1}, \Gamma_{qT}$) or ($\theta_{l1}, \Gamma_{\theta l}$; RH_1, Γ_{RH})

The initial linear shoreline sounding is a set of important external parameters for this model, we can either specify (θ_{e1}, $\Gamma_{\theta e}$; q_{T1}, Γ_{qT}) or (θ_{l1}, $\Gamma_{\theta l}$; RH_1, Γ_{RH}) as described in sec. 2.6.

Fig. 3.1.7 shows model runs using linear soundings of potential temperature (θ_e) and total water mixing ratio (q_T) at shore. A series of 4 different sets of initial shoreline sounding runs has been done in order to see how

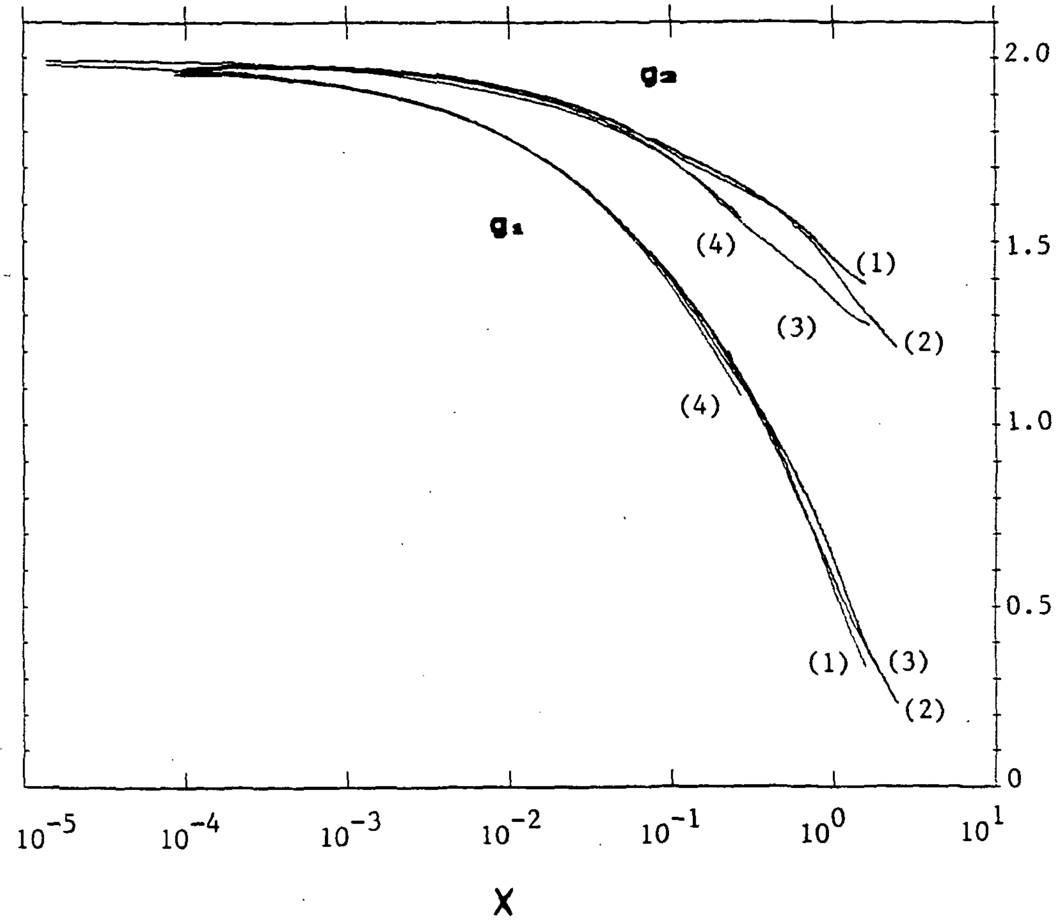

Fig.3.1.7 g_1 and g_2 as functions of X for various shoreline soundings. (see text)

the evolution of boundary layer is affected by the shoreline sounding. They are:

1. standard sounding except with θ_{e1} increased by 2°C,

2. standard sounding except with $\Gamma_{\theta e}$ = 3.0°C/km,

3. standard sounding except with q_{T1} increased by 1g/kg,

4. standard sounding except with Γ_{qT} = 0 g/kg/km,

where the standard sounding is the New York sounding as described in Table 3.1.1.

In Fig. 3.1.7, it is seen that the initial points of all these runs start off at different locations; this can be inferred from (2.4.13), (2,4.14b), and (2.2.19) that nondimensional fetch is affected by the changes of initial sounding data of θ_{e1}, q_{T1}, $\Gamma_{\theta e}$, Γ_{qT}. However, if the initial linear assumption of θ_1 and RH is used, then the changes of θ_{11}, RH_1, $\Gamma_{\theta 1}$, and Γ_{RH} can still affect θ_v and Γ_v, and these two parameters are the key factors to the changes of x_* and X.

The changes of g_1 and g_2 due to initial sounding parameters changes are in the range of 2% to 14% at any given fetch. Thus, it can be inferred that the horizontal heat and vapor transfer coefficients are not affected too much by the changes of initial soundings. More details are shown in Table 3.1.7.

We may also use another set of linear shoreline sounding assumptions in which θ_l and RH are assumed to be linear at the shore, with surface liquid water potential temperature $\theta_{l1} = 3.0^\circ C$ at shore and the lapse rate $\Gamma_{\theta l} = 3.8\ ^\circ C/km$. This is useful because it allows us to check the effects of relative humidity by running the model with a series of different shoreline surface relative humidities, $RH_1 = 0.2, 0.4, 0.6$, and 0.8, with the lapse rate $\Gamma_{RH} = 0.0$ g/kg/km.

One thing noticed from Fig. 3.1.8 is that the variations of g_1 caused by the changes of RH_1 are much smaller than those of g_2. From (2.4.8) to (2.4.16), g_2 is a function of λ and is directly affected by RH_1. Since λ becomes larger with a larger RH_1 from (2.4.12), so does g_2 and the changes of g_2 caused by RH_1 are significant. However, g_1 is not directly affected by RH_1, the changes of RH_1 cause variations of the rate of change of θ_{v1}, which will slightly change θ_{v1} and g_1.

Table 3.1.7

The changes of g_1 and g_2 caused by the changes of shoreline surface initial sounding parameters.

LogX	x (km)	Range of initial sounding parameters	Range of g_1 $(\bar{g}_1 \pm \Delta g_1)$	Range of g_2 $(\bar{g}_2 \pm \Delta g_2)$	Percent change in g_1 $(2\Delta g_1/\bar{g}_1)$	Percent change in g_2 $(2\Delta g_2/\bar{g}_2)$
-1.0	149-369	$\theta_e 1$: 11.5-13.5°C q_{T1}: 2.4-3.4g/kg	1.39±0.02	1.74±0.02	2.9%	2.4%
-0.5	472-510	$\Gamma_{\theta e}$: $(10^{-2}$°C/km) 1.925-3.0	1.07±0.01	1.59±0.05	1.9%	6.5%
0.0	1494-1612	Γ_{qT}: $(10^{-2}$g/kg/km) -0.75-0.0	0.60±0.04	1.40±0.06	13.8%	8.1%

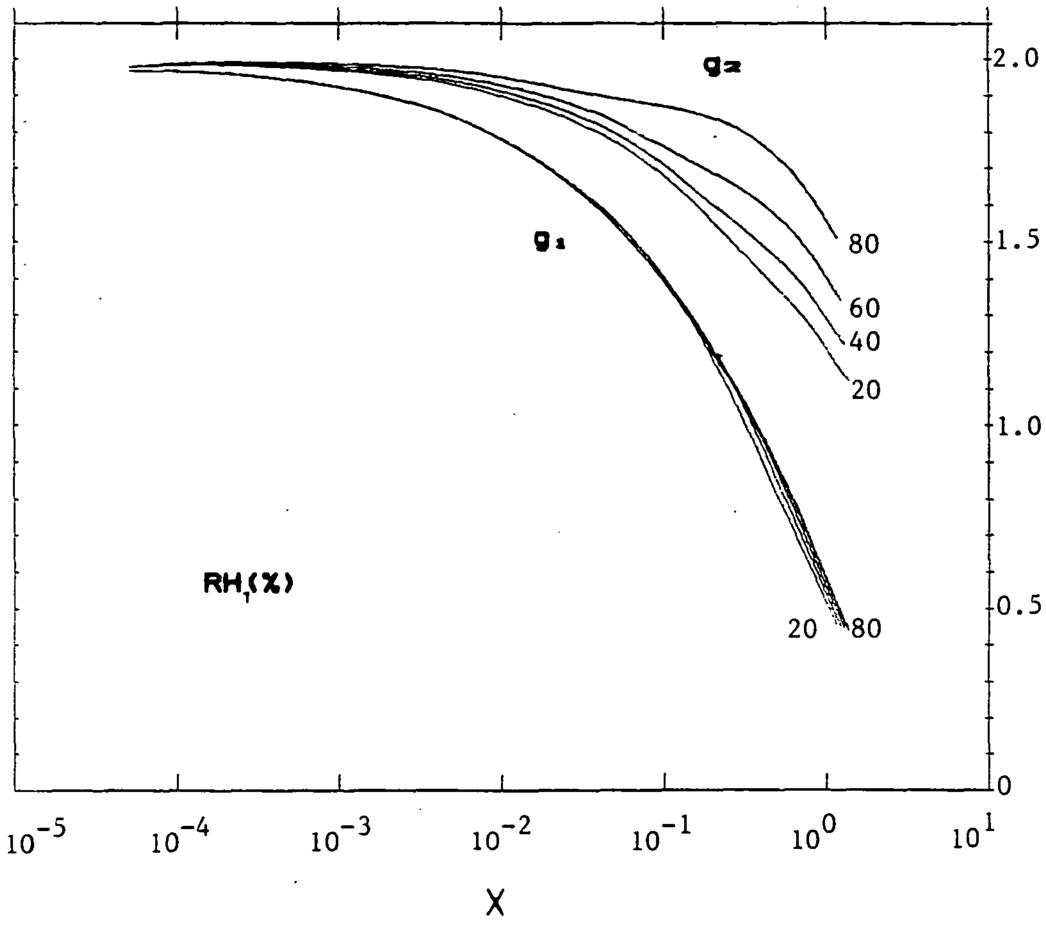

Fig.3.1.8 g_1 and g_2 as functions of X for various shoreline surface relative humidity. (RH_1: 20 to 80 %)

It is clearly seen that there are larger heat and vapor transfer coefficients at any given fetch when shoreline surface relative humidity is higher, this will tend to increase the surface heat and vapor fluxes. Meanwhile, the shoreline mixing ratio becomes larger with higher RH_1, this tends to decrease the surface surface fluxes. These two effects partly offset each other, and the surface fluxes are less senstive to the changes of RH_1. The variations of g_2 for the changes of RH_1 are much larger than the variations of g_1. Also, it is shown in Table 3.1.8 that the changes of both g_1 and g_2 increase with increased fetch. More details of the variations of g_1 and g_2 by the effects of shoreline surface relative humidity, RH_1, are shown in Table 3.1.8.

3.2 Summary of the Sensitivity Analysis

The analysis done in the last section shows that g_1 and g_2 are not very sensitive to external parameters when those parameters change within the range likely to be encountered during cold-air outbreaks. It is therefore possible to obtain accurate approximation of heat and vapor fluxes even when the data contain large errors.

Considering the New York sounding and a fetch of 600

Table 3.1.8

The changes of g_1 and g_2 caused by RH_1. RH_1: 0.2, 0.4, 0.6, and 0.8, with θ_{11} =3.0°C, $\Gamma_{\theta 1}$ = 3.8°C/km, Γ_{RH} = 0.0 g/kg/km.

LogX	x (km)	Range of RH_1	Range of g_1 $(\bar{g}_1 \pm \Delta g_1)$	 g_2 $(\bar{g}_2 \pm \Delta g_2)$	Percent change in g_1 $(2\Delta g_1/\bar{g}_1)$	 g_2 $(2\Delta g_2/\bar{g}_2)$
-1.0	186-193	0.2 to 0.8	1.40±0.01	1.77±0.09	1.5%	10.6%
-0.5	588-611	0.2 to 0.8	1.03±0.03	1.63±0.17	6.1%	20.4%
0.0	1859-1933	0.2 to 0.8	0.55±0.03	1.38±0.18	11.3%	25.6%

km (i.e. Log X ≅ -0.5). Table 3.2.1 shows the range of variation of g_1 and g_2 when each parameter is allowed to change by up to 50% from the New York sounding value.

In this chapter, the major findings of my research have been presented. From the results of my work, it can be inferred that the surface heat and moist fluxes for either cloud-free or cloud-topped regions can always be reasonably estimated by knowing the analytical values of g_1, g_2 at any fetch, the shoreline temperature lapse rate, and the surface temperature and mixing ratio differences between air over land and sea. This approximation should be reasonable accurate for all different soundings.

3.3 The Effect of External Parameters on the Horizontal Transfer Coefficients

In this section we look at the first (direct) and second (indirect) order effects of all external parameters on the horizontal transfer coefficients.

The independent variable of this marine atmosphere boundary layer (MABL) model is either time (t), or distance of fetch following the mean motion of air in the boundary layer (x). The relationship between t and x is:

Table 3.2.1.

The uncertainties of g_1 and g_2 caused by the errors of the external parameters at fetch equal to 600 km (The measurement errors are allowed to be up to 50%).

external data (w/ standard sounding values)	tolerance of data	range of parameters	resulting errors (fetch ≅ 600km) $(\bar{g}_1 \pm \Delta g_1)$ $(2\Delta g_1/\bar{g}_1)$	 $(\bar{g}_2 \pm \Delta g_2)$ $(2\Delta g_2/\bar{g}_2)$
Initial sounding:		(changes of) sounding data		
θ_{e1} (°C) 11.5,		11.5 to 13.5		
q_{T1} (g/kg) 3.4,		3.4 to 4.4	1.07±0.01 (1.9%)	1.59±0.05 (6.3%)
$\Gamma_{\theta e}$ (°C/km) 3.8,		3.0 to 3.8		
Γ_{qT} ($\frac{g/kg}{km}$) -0.75,		-0.75 to 0.0		

C-2

Table 3.2.1.(continued)

external data (w/ standard sounding values)		tolerance of data	range of parameters	resulting errors (fetch ≅ 600km) ($\bar{g}_1 \pm \Delta g_1$) ($2\Delta g_1/\bar{g}_1$)	 ($\bar{g}_2 \pm \Delta g_2$) ($2\Delta g_2/\bar{g}_2$)
U (m/sec)	16,	50%	8 to 24	1.01±0.02 (3.9%)	1.73±0.02 (2.3%)
D_1 (10^{-5}/sec)	4,	50%	2 to 6	0.96±0.06 (12.5%)	1.58±0.06 (7.6%)
D_2 (10^{-5}/sec)	4,	50%	2 to 6	0.84±0.03 (7.1%)	1.41±0.10 (13.5%)
T_o (°C)	12,		8 to 16	1.03±0.11 (21.4%)	1.72±0.03 (3.5%)
T_{sky}(°C)	-40,		-20 to -60	1.00±0.04 (8.0%)	1.72±0.02 (2.9%)
R_s (mK/sec)	0.1,	50%	.05 to .15	1.01±0.05 (9.9%)	1.72±0.03 (3.5%)
RH_1(%)	40,	50%	20 to 60	1.03±0.03 (6.1%)	1.55±0.08 (10.7%)

$$x = U t , \qquad (3.3.1)$$

where

U is the mean wind speed in MABL.

All the other dependent variables of the MABL are functions of either time or fetch. We will now look at the model evolution of these basic parameters of the boundary layer, e.g. θ_e, q_T.

First, the potential temperature change per unit time can be derived from (2.3.13), (2.3.14), and (2.3.16).

$$\frac{d\theta_e}{dt} = \frac{1}{Z_B} \left(\overline{W'\theta_e'}\Big|_0 + R_C - R_B + W_e \Delta\theta_e \right) \qquad (3.3.2)$$

where

$$\overline{W'\theta_e'}\Big|_0 = C_T U \left(\theta_{e0} - \bar{\theta}_e \right) \qquad (3.3.3)$$

In another expression, the temperature change per unit travel can be expressed as:

$$\frac{d\theta_e}{dx} = \frac{1}{U}\frac{d\theta_e}{dt} = \frac{1}{Z_B} \left(\frac{\overline{w'\theta_e'}\big|_0}{U} + \frac{W_e \Delta\theta_e}{U} + \frac{R_c}{U} - \frac{R_B}{U} \right) . \qquad (3.3.4)$$

Then, from (3.3.3), (3.3.4) can be written as:

$$\frac{d\theta e}{dX} \cong \frac{1}{Z_B}\left(C_T(\theta_{Mo}-\theta_M)+\frac{We\Delta\theta}{U}+\frac{R_C}{U}-\frac{R_\theta}{U}\right) . \qquad (3.3.5)$$

From (3.3.2) to (3.3.5), it is proven that wind speed (U) has first order effect on the changes of temperature per unit time and travel; surface heat fluxes per unit time; radiation warming, cooling and entrained heat fluxes per unit travel. However, the wind speed has only second order effect on surface heat fluxes per unit travel.

Similarly, the rate of change of total water mixing ratio per unit time can be derived from (2.3.12), and (2.3.15).

$$\frac{dq_T}{dt} = \frac{1}{Z_B}\left(\overline{W'q_T'}|_o + W_M \Delta q_T \right), \qquad (3.3.6)$$

where

$$\overline{W'q_T'}|_o = C_M U(q_o - \bar{q}_T) , \qquad (3.3.7)$$

and then the mixing ratio change per unit travel can be expressed as:

$$\frac{dq_T}{dx} = \frac{1}{U}\frac{dq_T}{dt} = \frac{1}{Z_B}\left(C_q(q_o - q_T) + \frac{W_e \Delta q}{U}\right) \qquad (3.3.8)$$

A similar conclusion could be obtained using (3.3.7) through (3.3.10). The wind speed has first order effect on the change of total water mixing ratio per unit time and travel, surface water vapor fluxes per unit time. and entrained vapor fluxes per unit travel. However, it has second order effect on the surface water vapor fluxes per unit travel.

From, (2.4.3), (2.4.4), and (2.4.5), g_1 and g_2 can also be expressed as:

$$g_1 = \frac{\rho C_p}{C_1 x(\theta_{vo} - \theta_{vi})} \int_0^x C_T(\theta_{eo} - \theta_e)\, dx \,, \qquad (3.3.9)$$

$$g_2 = \frac{\rho L}{C_2 x(q_o - q_{Ti})} \int_0^x C_q(q_o - q_T)\, dx \,, \qquad (3.3.10)$$

As is concluded that wind speed does not directly affect the surface heat and vapor fluxes per unit travel. It is also seen from (3.3.9) and (3.3.10) that g_1 and g_2 are not directly affected by wind speed. However, wind speed does indirectly affect g_1 and g_2, because the rates of change of θ_m and q_T are affected by wind speed (from (3.3.2) and (3.3.6)). This has also been identified in Fig. 3.1.1, which shows that when wind speed is large the changes of g_1 and g_2 are small with respect to the variations of wind speed; and when wind speed is small, the changes of g_1 and g_2 are much larger. There is no linear relationship between wind speed and horizontal transfer coefficients. This also tells that wind speed has second order effect on the horizontal transfer coefficients.

In a more generalized conclusion, from (3.3.2) and (3.3.6), it can be inferred that all the external parameters have a second order effect on the surface heat and vapor fluxes per unit travel, i.e. the horizontal transfer coefficients.

In the next section, the strengths and weaknesses of this numerical boundary layer method will be discussed, and some further research direction in this area will be discussed in the next chpater.

3.4 Model Strengths and Weaknesses

In Chapter 2 and 3, we have compared the results of analytical and numerical solutions of the marine atmosphere boundary layer evolution and studied the evolution of the horizontal transfer coefficients with respect to the boundary layer external parameter variation. In conclusion, the strengths and weaknesses of the modified numerical model will be discussed in this section.

The analytical solution derived by Stage (1983a) is valid only for the dry boundary layer, cloud-free cases. While the numerical integration method presented in this paper not only provides an identical solution to the analytic solution of dry boundary layer case (sec. 2.5), it also presents a method to estimate the solution for the wet, cloud formed, boundary layer condition.

Hence, the most significant point of the theoretically accurate numerical method is that it provides an easy way of computing the MABL heat and vapor fluxes during cold-air outbreaks. It is good for both before and after cloud formation during boundary layer evolution, and it is much more applicable to the real atmosphere stratus topped boundary layer conditions than is the analytic model.

Another noticeable strength of this numerical model is that it can predict the estimated boundary layer evolution from conveniently available data sources, such as the shoreline sounding parameters ((θ_{e1}, $\Gamma_{\theta e}$, q_{T1}, Γ_{qT}), wind speed (U), divergences (D_1, D_2)), and satellite measurable parameters (water surface temperature (T_o), and radiative sky temperature (T_{sky})).

The changes of the predicted values of horizontal heat and vapor transfer coefficients are quite small with respect to the wide range changes of measured external boundary layer parameters, as has been shown in Section 3.5.

Therefore, by using this numerical method, we can afford to have large measurement errors of the sounding or satellite data, and still come out with reasonably accurate estimates of the boundary layer heat and vapor fluxes input from the warm water surface.

On the other hand, because this model is based on the idealized initial condition for analytic solution, there are also some constraints on this numerical method. As mentioned in Chapter 2, the idealized initial assumptions of horizontal homogeneous state in the shoreline direction, linear boundary layer profiles often do not exist in real atmospheric boundary layers.

Also, if the contrast in temperature between the water surface and the air is not large enough, buoyant production is no longer dominant, and a more complicated MABL model which includes the shear production will be needed. The horizontal homogeneous assumption in the shoreline direction is also quite severe. It oversimplifies the boundary layer evolution in the shoreline direction, and the computation of surface heat and vapor fluxes per unit area from the warm water surface.

Furthermore, this model is not complete enough to include the conditions of free entrainment on the top of the boundary layer, radiation warming at cloud top, and radiation cooling at the cloud base. As mentioned in Section 3.4, this numerical model will be terminated once these additional situations above are encountered.

For further studies in this area of MABL evolution during cold air outbreak episodes, all the critical conditions discussed above must be included in this model also. Therefore, further development of a more generalized complete numerical model to closely simulate the real atmospheric situations need to be done in future endeavors.

CHAPTER 4. Conclusions and Outlook

Stage and Businger (1981a,b) first proposed the MABL model which simulates the growth and evolution of a cloud-topped boundary layer during cold-air outbreaks. This thesis using the modified version of Stage and Businger's model numerically studies the surface heat and vapor fluxes into the boundary layer. Several significant results have been found through the study of this paper.

Chou and Atlas (1982) first proposed and proved the idea of horizontal transfer coefficients for the cloud-free region. This is a new kind of parameterization for the convectively unstable boundary layer case, which depends on the horizontal temperature and mixing ratio differences across the coast, instead of the vertical differences as in the classical bulk transfer formulas. Through the present work this idea has been extended from cloud-free regions into cloud-topped regions. The horizontal heat (g_1) and vapor (g_2) transfer coefficients numerically estimated by the modified MABL model have been proven to be identical to the analytical solutions by

Stage (1983a) for the dry (cloud-free) case, and also can be applied to the wet (cloud-topped) case. Thus, the numerical MABL model simulates the marine boundary layer surface fluxes more realistically than the analytical method does when stratus clouds are present in the upper boundary layer. In addition, from my work it is found that the changes of g_1 and g_2 are not very sensitive to the changes of those sounding memasurable external parameters.

Nevertheless, the most significant conclusion can be inferred that the estimates of g_1 and g_2 at any given fetch should always be reasonably accurate for any given soundings by using the analytical (dry boundary layer) solutions figure of g_1 and g_2 (Fig. 2.5.2, or Fig. 2.5.3). The values of fetch can be computed from the shoreline sounding temperature lapse rate, and the surface temperature differences between air at shore and sea. Hence, the surface heat and vapor fluxes at any given fetch and the total fluxes from shore to any value of fetch in the boundary layer, cloud-free or cloud-topped, are easily obtained.

Since only a few initial shoreline sounding data are required for the run of simulating the boundary layer evolution, it is also recommended to actually run this MABL model numerically if more accurate results are desired. Therefore, the actual values of g_1 and g_2 and total fluxes can be obtained from the numerical model results, which are very good estimates even with some large sounding measurement errors as discussed early in Chapter 3.

The boundary layer is an important link of energy budgets between the oceanic and atmospheric circulations. Further work in this area should include a more detailed evaluation of distribution of the energy source from the water (i.e. the buoyancy production of Turbulent Kinetic Energy); how much of this energy is dissipated by the eddies of the boundary layer; how much is used to drive the entrainment process; and how much is carried up beyond the boundary layer to serve as an energy input for the atmosphere circulation. Atlas and Chou's (1983) studies of the feedback effects from ocean to the low level mesoscale circulation in the Northern Atlantic winter suggested that the atmospheric circulations are greatly affected by the boundary layer surface heat and vapor fluxes from water. Further studies in this area will be very useful for the energetics of cyclogenesis during winter time storms over warm water surfaces, such as Northern Atlantic, Northern Pacific ocean and East China sea winter low pressure system regions.

A more generalized MABL model which should include not only the buoyancy production, but also the shear production. This model could simulate the boundary layer evolution for any well mixed layer, i.e. the buoyancy dominant unstable layer, or the near neutral layer as long as the shear term is strong enough to keep the layer well mixed.

Overall, the most important topic for future research should be emphasized on how the oceanic heat and vapor fluxes contribute to the energy and vorticity of atmosphere circulation by passing through boundary layer during the cold-air outbreaks episodes. A more complete numerical model including the Turbulent Kinetic Energy equation and the Turbulent Vorcity Budget equation might be able to offer some clues to solve this problems of future endeavors.

REFERENCES

Allison, D. E., 1984 : A model for the estimation of the surface fluxes of momentum, heat, and moisture of the cloud topped marine atmospheric boundary layer from satellite measurable parameters. M.S. thesis, Department of Meteorology, Florida State University, 66pp.

Atlas, D. and S. H. Chou, 1983 : The influence of coastal shape on winter mesoscale air-sea interaction. *Mon. Wea. Rev.* *111*, 245 - 252.

Ball, F. K., 1960 : Control of inversion height by surface heating. *Quart. J. Roy. Met. Soc.* *86*, 483 - 494.

Chou, S. H., and D. Atlas, 1982 : Satellite estimates of ocean-air heat fluxes during cold air outbreaks. *Mon. Wea. Rev.* *110*, 1434 -1450.

Deardorff, J. W., 1976 : On the entrainment rate of a stratocumulus-topped mixed layer. *Quart. J. Roy. Met. Soc.* *102*, 563 - 582.

Ninomiya, K., 1974 : Bulk properties of cumulus convections in the small area over Kuroshio region in February 1968. *J. Meteor. Soc. of Japan.* *52*, 188 - 203.

Ninomiya, K. 1975 : Large-scale aspects of air-mass transformation over the East China sea during AMTEX'74. J. Meteor. Soc. of Japan. 53, 285 - 303.

Ninomiya, K., and T. Akiyama, 1976 : Structure and heat energy budget of mixed layer capped by inversion during the period of polar outbreaks over Kuroshio region. J. Meteor. Soc. of Japan. 54, 160 - 174.

Stage, S. A., 1979 : A model for modification of the cloud-topped marine boundary layer during cold-air outbreaks. Ph.D. dissertation, University of Washington, 280pp.

Stage, S. A., and J. A. Businger, 1981a : A model for entrainment into a cloud-topped marine boundary layer. Part I: Model description and application to a cold-air outbreak episode. J. Atmos. Sci. 38, 2213 - 2229.

Stage, S. A., and J. A. Businger, 1981b : A model for entrainment into a cloud-topped marine boundary layer. Part II: Discussion of model behavior and comparison with other models. J. Atmos. Sci. 38, 2230 - 2242.

Stage, S. A., 1983a : Boundary layer evolution in the region between shore and cloud edge during cold-air outbreaks. J. Atmos. Sci. 40, 1453 - 1471.

Stage, S. A. 1983b : Factors influencing the marine boundary layer during a cold air outbreak. Boundary layer meteo. 26, 269 - 287.